Home Search Collections Journals About Contact us My IOPscience

General phenomenology of ionization from aligned molecular ensembles

This content has been downloaded from IOPscience. Please scroll down to see the full text.

2015 New J. Phys. 17 023069

(http://iopscience.iop.org/1367-2630/17/2/023069)

View the table of contents for this issue, or go to the journal homepage for more

Download details:
This content was downloaded by: phockett
IP Address: 132.246.113.196
This content was downloaded on 25/02/2015 at 15:27

Please note that terms and conditions apply.

New Journal of Physics
The open access journal at the forefront of physics

Deutsche Physikalische Gesellschaft DPG
IOP Institute of Physics
Published in partnership with: Deutsche Physikalische Gesellschaft and the Institute of Physics

CrossMark

OPEN ACCESS

RECEIVED
23 May 2014

REVISED
8 September 2014

ACCEPTED FOR PUBLICATION
26 January 2015

PUBLISHED
24 February 2015

Content from this work may be used under the terms of the Creative Commons Attribution 3.0 licence.

Any further distribution of this work must maintain attribution to the author (s) and the title of the work, journal citation and DOI.

PAPER

General phenomenology of ionization from aligned molecular ensembles

Paul Hockett
National Research Council of Canada, 100 Sussex Drive, Ottawa, K1A 0R6, Canada
E-mail: paul.hockett@nrc.ca

Keywords: molecular alignment, ionization, multiphoton processes, photoelectron angular distributions

Abstract

Single and multi-photon ionization of aligned molecular ensembles is examined, with a particular focus on the link between the molecular axis distribution and observable in various angle-integrated and angle-resolved measurements. To maintain generality the problem is treated geometrically, with the aligned ensemble cast in terms of axis distribution moments, and the response of observables in terms of couplings to these moments. Within this formalism the angular momentum coupling is treated analytically, allowing for general characteristics—independent of the details of the ionization dynamics of a specific molecule—to be determined. Limiting cases are explored in order to provide a phenomenology which should be readily applicable to a range of experimental measurements, and illustrate how observables can be sensitive to fine details of the alignment, i.e. higher-order moments of the axis distribution, which are often neglected in experimental studies. We hope that this detailed and comprehensive treatment will bridge the gap between existing theoretical and experimental works, and provide both quantitative physical insights and a useful general phenomenology for researchers working with aligned molecular ensembles.

1. Introduction

Over the last decade techniques for molecular alignment have become increasingly advanced, and increasingly popular. Perhaps the most common, and experimentally accessible, technique is non-adiabatic (or impulsive) alignment, achieved via the interaction of a short, intense laser pulse with a rotationally cold, gas phase sample [1–5]. In the case of an IR driving field, multiple cascaded Raman transitions occur during the pulse, populating many rotational levels, thereby creating a broad rotational wavepacket in the system. After the pulse, the wavepacket propagates under field-free conditions, and undergoes revivals at characteristic times, determined by the rotational constants of the molecule. The utility of this type of alignment—as compared to adiabatic alignment techniques—is that further experiments may be carried out in the vicinity of the revivals, thus providing field-free conditions for these measurements, albeit on a highly rotationally excited system.

Recent examples of the application of this technique span a wide gamut of measurements, including weak and strong-field photoelectron angular distributions (PADs) for probing dynamics [6–8] or 'approaching the molecular frame (MF)' [9–13], high-harmonic measurements [14–19], angle-resolved ATI [20, 21], Coulomb explosion [13, 22, 23] and x-ray diffraction [24] to mention just a few examples. In most cases the application of alignment is at the qualitative level, where the alignment is optimized based on a proxy for the degree of alignment (e.g. ionization yield at a revival feature of the rotational wavepacket [21, 25]), and the experimental goal is to maximize the alignment effect, or observe some phenomena which would otherwise be obscured by orientational averaging—for instance imaging torsional motions [26]. In other cases, the aim is a more quantitative study of the rotational wavepacket behaviour [25, 27], or detailed understanding of MF phenomena which can be directly observed if the degree of alignment is high [24], or may be 'extracted' from measurements in the lab frame in certain cases provided the alignment is well-characterized and the coupling to the observable well-understood [17, 28–30].

© 2015 IOP Publishing Ltd and Deutsche Physikalische Gesellschaft

In terms of a qualitative approach, the degree of alignment is often considered solely in terms of $\langle \cos^2\theta \rangle$ (the expectation value of $\cos^2\theta$), where θ is the angle between the molecular axis and lab frame z-axis [4], and this metric is treated as completely defining the axis distribution in the lab frame. For a fuller treatment of the molecular axis distribution, higher-order moments of the distribution (e.g. $\langle \cos^n\theta \rangle$) must be taken into account. For example, PADs are known to be sensitive to higher-order alignment moments [28, 31]. This response of higher-order observables to higher-order alignment moments has long been implicit in work on photoionization, and was first discussed explicitly in the context of recent work on rotational wavepackets by Seideman [32] and Underwood and Reid [28]. Some of the implications of this coupling have been investigated extensively in theory work from Seideman and co-workers [27, 30, 31, 33], the most recent of which discusses the possibility of mapping alignment via measurement of PADs as well as the use of other probe techniques.

Regardless of the aims of a given study, but of particular importance in experiments seeking MF properties, is the detailed understanding of the probe process, and the response of the observable to the degree of alignment. At a basic level this is required to formulate metrics to optimize the degree of alignment and interpret results in terms of the underlying properties of interest. In the lowest-order approach, the optimum alignment corresponds to maximizing $\langle \cos^2\theta \rangle$ and, practically, such optimization typically takes the form of maximizing the contrast observed between the alignment and anti-alignment features of a revival of the rotational wavepacket. However, depending on the observable, the contrast may be poor or negligible, even in the presence of a highly aligned distribution, negating the use of such signals as a measure of alignment[1]. In these cases a more detailed treatment of the alignment may be necessary for even a qualitative interpretation of experimental results.

At a more detailed level one might hope to fully characterize the aligned distribution, allowing for more quantitative analysis of experimental data. This is a non-trivial task but, despite the complications, such detailed analysis has been attempted in a few cases, for example [8, 13–15, 20, 25, 29] all illustrate detailed analyses of the prepared alignment and various molecular properties. In tandem with the experimental efforts, various *ab initio* studies have also presented results for specific molecules and types of measurements (see, for example, [27, 34–37]). It is interesting to note that in many cases (e.g. single photon ionization, fluorescence) the fundamentals have long been known, but have only been applied in older studies where static alignments, or narrow rotational wavepackets, were prepared[2].

In this work we also investigate the response of observables in photoionization experiments to aligned distributions, and approach the problem quite generally from a geometric perspective. A geometric approach allows for the separation of the molecular axis distribution from other, molecule specific, properties [28, 38, 39]. We thus aim to provide a useful and general applied phenomenology which can provide qualitative and quantitative insights into the ionization of aligned distributions. This treatment begins with the formalism of Underwood and Reid [28] (which was further discussed and extended in Stolow and Underwood [39]), from this we derive and discuss explicit forms for typical experimental measurements. We further extend the formalism to N-photon ionization, in order to discuss the link between single and multi-photon ionization processes, including both angle-integrated and angle-resolved observables. Typically, single and multi-order processes are treated independently by the 'weak' and 'strong' field communities despite the similarities of the underlying physical processes, so such a treatment may be useful in bridging this divide in some cases[3]. Using the formalism presented we explore the general form of different experimental measurements—specifically angle-integrated ionization yields as a function of pump–probe polarization geometry, polarization-angle resolved measurements, and angle-resolved photoelectron measurements—and, by incorporating rotational wavepacket calculations for an example system under typical experimental conditions, investigate limiting cases, providing an aid to experimentalists working to prepare and optimize aligned distributions.

Although some aspects of this work are extant in the literature and known by practitioners in either the alignment community or the photoionization community, not to mention other fields which make use of strong-field alignment (as noted above), the complexity of the wavepacket and observables have resulted in very few works which cross-over between these fields and cover all aspects from wavepacket to observable. Notable exceptions are experiments from Suzuki and co-workers [7, 8, 40], and theory from Underwood and Reid [28], and Seideman and co-workers [27, 30, 32, 41]. In a following paper [42] we apply our formalism to ionization of aligned butadiene and compare theory with experimental results; hence, we aim here to provide complementary insights and more direct comparison to experiment than existing studies, as well as a unified and generalized geometric treatment of the relevant theory. Most generally, we aim to bridge the gap between theoretical understanding of the physics, notably the angular momentum coupling between the axis distribution and the observables, and experiments where one must treat specific cases, usually with many unknowns, in particular the precise, molecule-specific details of the probe process.

---

[1] The illustration of this effect is one of the purposes of the current work, but we note in passing that this issue is discussed in terms of photoelectron yields in [58], wherein a certain choice of ionization parameters was shown to result in effectively no response of the yield to molecular axis alignment, and in terms of ion fragment yields in [2], wherein different fragment channels were found to exhibit markedly different revival contrast. In this latter case, the observation was ascribed to the ionization channel dependence on probe laser intensity and concomitant focal-volume averaging effects.

[2] We note for completeness that there is a strong relation of much recent work to rotational coherence spectroscopy (RCS), as developed by Felker and Zewail [72]. The primary difference between older and more modern alignment techniques is the preparation of the rotational wavepacket using strong IR pulses, leading to much broader rotational wavepackets than those created via single (or few) photon absorption. Additionally, the low-order observables in RCS render the observed signals sensitive to only low-order moments of the aligned distribution. Similar comments hold when comparing frequency-resolved photoionization measurements to time-resolved measurements: the underlying physics in terms of rotational couplings is identical, but the narrow rotational distributions prepared are phenomenologically quite different.

[3] It is the case, however, that the treatment developed here is strictly valid only in the perturbative regime, so can only be assumed to be qualitative in the true strong-field regime. For multi-photon processes at moderate intensities, however, it should be applicable.

2. Theory

The necessary theory for a full treatment of molecular alignment and ionization is discussed here, with a focus on quantification of the relevant parameters. We begin by treating the aligned distribution geometrically for the most general case (full 3D axis alignment), and the simpler cases of 2D or 1D distributions which are applicable to symmetric top and linear molecules, and experimental configurations with cylindrical symmetry. We then consider parametrization of alignment in detail, and the coupling of these alignment metrics into ionization measurements, for single and multi-photon ionization processes, including frame rotations and the response of the observables in typical experimental measurements. Throughout example calculations are used to illustrate the equations, and investigate limiting cases, which are further discussed in section 3.

2.1. Axis distribution moments (ADMs)

We begin with a description of the spatial distribution of molecular axis. Most generally, the distribution should be described by an expansion in 3D functions, specifically the Wigner rotation matrices [39]:

$$P(\varOmega,\, t) = \sum_{K,Q,S} A^{K}_{Q,S}(t) D^{K}_{Q,S}(\varOmega), \tag{1}$$

where $\varOmega = \{\varPhi,\, \varTheta,\, \chi\}$ are the Euler angles describing the position of the molecular axis relative to a reference frame, $D^{K}_{Q,S}(\varOmega)$ are Wigner rotation matrices and $A^{K}_{Q,S}(t)$ are expansion parameters which are generally termed the ADMs and, for dynamical systems, may be time-dependent. The quantum numbers K, Q, S denote the rank/moment of the distribution, and projections onto the space and body-fixed axis respectively.

The general form of the distribution can be simplified for the case of linear and symmetric top molecules, for which $S = 0$ only, and the Wigner matrices can be replaced with an expansion in 2D functions:

$$P(\theta,\, \phi,\, t) = \sum_{K,Q} A_{K,Q}(t)\, Y_{K,Q}(\theta,\, \phi), \tag{2}$$

where $Y_{K,Q}(\theta,\, \phi)$ are spherical harmonics. (Throughout this manuscript we use upper-case $\varTheta$, $\varPhi$ for Euler angles, and lower-case θ, ϕ for spherical polar coordinates although, in many cases, the angles are referenced to the same axis, hence are identical.)

In the case of a cylindrically symmetric distribution, for which $Q = 0$, a further simplification to use 1D functions can be made:

$$P(\theta,\, t) = \sum_{K} A_K(t)\, \mathscr{P}_K(\cos(\theta)), \tag{3}$$

where $\mathscr{P}_K(\cos(\theta))$ are Legendre polynomials in $\cos(\theta)$, and normalization factors relative to the spherical harmonic expansion above are subsumed into the A_K.

In practice, the laboratory frame (LF) of reference polar axis (z) is chosen to be defined by the laser polarization axis for linearly polarized light, or the propagation axis for elliptically (or pure circularly) polarized light, of the (pump) laser pulse used to prepare the aligned sample. In the former case the axis distribution is constrained to be cylindrically symmetric, and in both cases there is reflection symmetry along the polar (z) axis, so $K = 0, 2, 4, 6\ldots.K_{\mathrm{max}}$ (odd K can only appear in the case of an oriented distribution).

In the remainder of this work we restrict our discussion to the case of linearly polarized laser pulses for simplicity, although the formalism given here can be applied to any arbitrary polarization state. For linearly polarized light the axis distributions are defined by the cylindrically symmetric $P(\theta, t)$, as given by equation (3), although the symmetry may be broken in the case of a frame rotation between pump and probe pulses (see below), which can lead to a ϕ dependence of the axis distribution in the probe reference frame. To allow for this, we use the spherical harmonic expansion given by equation (2) as the more general definition throughout this

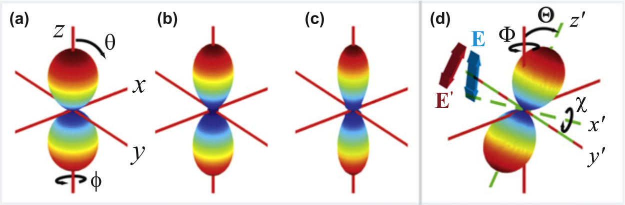

Figure 1. Example axis distributions $P(\theta, \phi)$ for distributions with (a) $A_{2,0} = 1$, (b) $A_{2,0} = 1,\ A_{4,0} = 0.4$ and (c) $A_{2,0} = 1,\ A_{4,0} = 0.4,\ A_{6,0} = 0.3$. (d) shows the distribution in (a) after a frame rotation of Θ between the pump (alignment) pulse and the probe (ionization) pulse, with polarization vectors $\mathbf{E}'$ and $\mathbf{E}$ respectively; the polarization geometry of the measurement is thus defined by Θ. The spherical polar coordinate system (θ, ϕ) and the Euler angles $\Omega = \{\Phi, \Theta, \chi\}$ are also shown in (a) and (d) respectively.

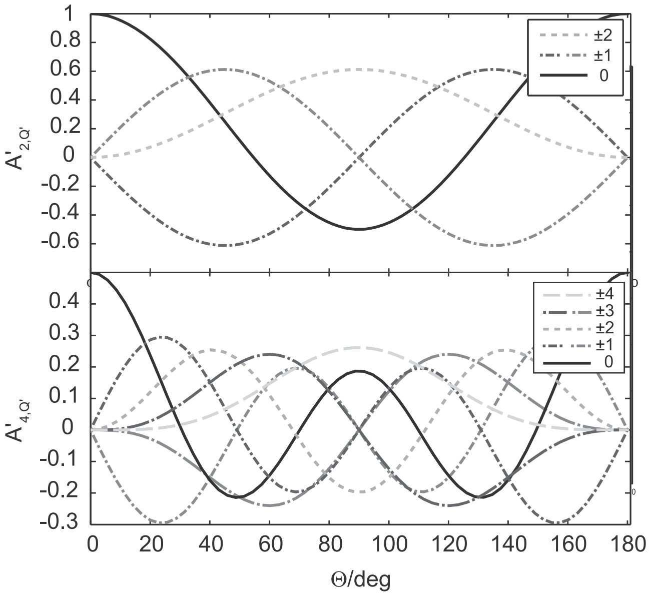

Figure 2. Behaviour of axis distribution moments $A'_{K,Q'}$ under frame rotation of Θ for a distribution with $A_{2,0} = 1,\ A_{4,0} = 0.5$ in the initial, unrotated frame ($\Theta = 0$). Note that curves for $\pm Q'$ are sign invariant for even Q'.

work, even when discussing cylindrically symmetric distributions ($Q = 0$, no ϕ dependence), but omit the ϕ label in cylindrically symmetric cases.

Examples of cylindrically symmetric axis distributions with increasing $K_{\max}$ are shown in figures 1(a)–(c), and the effect of a frame rotation between pump and probe polarization axis for linearly polarized pulses is shown in figure 1(d).

The effect of a frame rotation from pump to probe frames, as illustrated in figure 1(d), can be expressed in terms of the original and final ADMs and the rotation matrix element which transforms between the frames according to the set of Euler angles Ω:

$$A'_{K,Q'}(t;\,\Omega) = \sum_{K}\sum_{Q} D^{K}_{Q',Q}(\Omega) A_{K,Q}(t), \tag{4}$$

$$= \sum_{K} D^{K}_{Q',0}(\Omega) A_{K,0}(t), \tag{5}$$

where the second line includes the assumption that $Q = 0$, i.e. the initial distribution is cylindrically symmetric. Even in the case of such a distribution, the probe frame may contain terms with $Q' \neq 0$. Figure 2 shows the application of a frame rotation by Θ on the ADMs illustrated in figure 1(b) ($A_{2,0} = 1, A_{4,0} = 0.5$). Such rotations are important for consideration of the mapping of rotational wavepackets, and the understanding of angle-resolved measurements, since they appear through the dependence of the observable on the polarization geometry of the measurement.

2.2. Rotational wavepackets

In order to calculate the axis distributions defined geometrically above, for a specific molecular system, knowledge of the rotational wavefunction is required. In alignment experiments as discussed above, a rotational wavepacket $\psi(t)$ is prepared via interaction with an intense IR pump laser pulse, and then evolves under field-free conditions.

The axis distribution is determined by the projection of this wavefunction onto the Euler angles $\hat{\Omega}$, and integrated over the unobserved angles. For the cylindrically symmetric case (i.e. Φ and χ are summed over) this is given by [43]:

$$P(\theta, t) = \iint_0^{2\pi} \left| \left\langle \hat{\Omega} \middle| \psi(t) \right\rangle \right|^2 \mathrm{d}\Phi \mathrm{d}\chi. \tag{6}$$

The rotational wavefunction can be expanded in the symmetric-top basis:

$$|\psi(t)\rangle = \sum_J c_J(t) |JKM\rangle, \tag{7}$$

where J, K and M are the usual symmetric-top quantum numbers, denoting rotational angular momentum J and projections K and M onto the molecular and LF z-axis respectively; t is the time, where $t = 0$ (henceforth denoted t_0) is defined by the peak of the pump laser pulse and the end of the laser pulse by t_f; the $c_J(t)$ are the expansion coefficients.

Because the $|JKM\rangle$ state populations do not change after the interaction with the laser pulse, all field-free temporal evolution of the axis distribution ($t > t_f$) is contained in the phase of the c_Js, and is given by:

$$c_J(t) = c_J\left(t_f\right) \mathrm{e}^{2\pi E_J t} \tag{8}$$

The calculation of $P(\theta, t)$ therefore depends on the calculation of the $c_J(t)$, which requires knowledge of the rotational energy levels E_J and the $c_J(t_f)$. This final aspect, determined by the light–matter interaction during the pump laser pulse ($t < t_f$), must be treated numerically and is discussed in appendix A.

In this work we use butadiene as a specific example, and base calculations of $P(\theta, t)$ on 'typical' experimental conditions (peak intensity $(I) = 5$ TW cm^{-2}, pulse length $(\tau) = 400$ fs, rotational temperature $(T_r) = 2$ K), chosen to correspond to recent experimental work on butadiene (which will be discussed in a later publication [42]). In the calculations we assume a symmetric top molecule, the relevant rotational constants and polarizabilities for butadiene are given in appendix A. The calculated $P(\theta, t)$ in this case is shown in figure 3, in both Cartesian and polar forms[4]. Full discussion of the results, and the coupling of $P(\theta, t)$ into the observables defined in the remainder of this section, can be found in section 3; here we note simply that the distribution exhibits a high degree of spatial anisotropy, with population heavily weighted to the poles, indicating high-order $A_{K,Q}$ terms are present (see the low-order distributions shown in figure 1), and evolves rapidly along the temporal coordinate.

2.3. Alignment metrics

As discussed above, the degree of alignment is often quantified and reported in the literature in terms of $\langle\cos^2(\theta, t)\rangle$, the expectation value of $\cos^2(\theta)$ at time t. This metric of the axis alignment is defined by [43, 44]:

$$\begin{aligned}\langle\cos^2(\theta, t)\rangle &= \sum_{J,K,M,J'} \langle\psi(t)|\cos^2(\theta)|\psi(t)\rangle \\ &= \sum_{J,K,M,J'} c_{J'}^{*}(t) c_J(t) \langle J'KM|\cos^2(\theta)|JKM\rangle,\end{aligned} \tag{9}$$

where the matrix element can be calculated analytically. The expectation value can also be written in terms of the axis distribution. For the 1D case this is given by:

$$\langle\cos^2(\theta, t)\rangle = \int_0^{2\pi} \cos^2(\theta) P(\theta, t) \mathrm{d}\theta. \tag{10}$$

Thus $\langle\cos^2(\theta, t)\rangle$ can be obtained directly from the wavefunction, or extracted from the full axis distribution by projection onto $\cos^2(\theta)$. This is just another way of obtaining a second-order moment of the axis distribution, expressed in a cosine basis. By use of equations (1)–(3), selected according to the dimensionality of the problem, the moments obtained in this fashion can also be directly related to the ADMs for any order expectation value

---

[4] For clarity, we note that although asymmetric tops are covered by the analytical framework discussed above, due to the symmetric top treatment employed numerically the results illustrated here will not show any effects associated with asymmetric top rotational wavepacket dynamics [68].

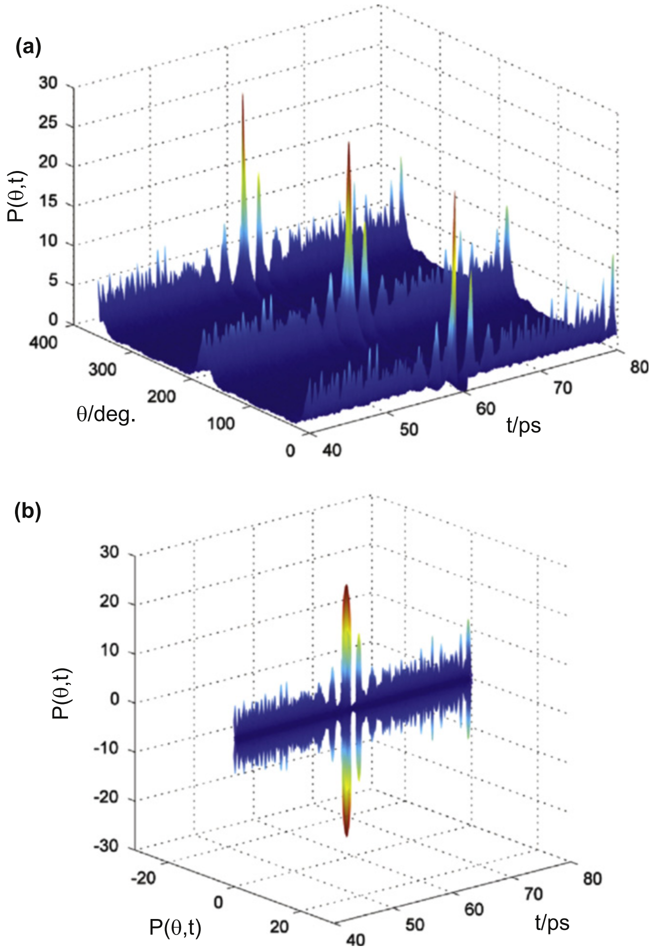

Figure 3. Calculated $P(\theta, t)$ for butadiene in the vicinity of the half-revival of the rotational wavepacket, results are shown as (a) Cartesian plot and (b) polar plot.

$\cos^n(\theta)$. Continuing with the 1D case (equation (3)), this yields:

$$\langle \cos^n(\theta,\ t) \rangle = \sum_K A_K(t) \int_0^{2\pi} \cos^n(\theta) \mathscr{P}_K(\cos(\theta))\, \mathrm{d}\theta. \tag{11}$$

The $\langle \cos^n(\theta) \rangle$ are therefore a linear combination of the ADMs, weighted by the overlap integral for each K. From these considerations, it is clear that the use of $\langle \cos^2(\theta,\ t) \rangle$ as a metric for characterizing an aligned distribution depends on the exact characteristics of $P(\theta, t)$. Distributions with significant high-order $A_{K,Q}$ may not be well-described by $\langle \cos^2(\theta,\ t) \rangle$ alone. Similarly, the nature of the probe process will dictate whether higher-order terms are coupled into the observable, providing a second criterion for the necessity of higher-order terms. Although this point has been discussed before in the literature (e.g. [31]), it appears to be the case that most work on aligned distributions considers only the second-order $(\cos^2(\theta,\ t))$ moment, so demonstration of the effects of higher-order moments remains a significant motivation in this work. For non-cylindrically symmetric cases, expectation values of $\cos^2$ for other angles are also used to quantify the full 3D alignment [44, 45], and recently a single metric for 3D alignment based on this has been proposed [46]; naturally these metrics will similarly be of best utility for probe process insensitive to higher-order moments of the distribution.

Continuing the concrete example of a wavepacket calculation for butadiene (treated as a symmetric top), as sketched above and illustrated in figure 3, the corresponding alignment metrics $\langle \cos^2(\theta,\ t) \rangle$ and $A_{2,0}(t)$ are shown in figure 4. Here $\langle \cos^2(\theta,\ t) \rangle$ was calculated directly from the rotational wavefunction, as defined in equation (9), while $A_{2,0}(t)$ was found by fitting the calculated $P(\theta, t)$ to an expansion in spherical harmonics, as defined in equation (2). In this case the temporal response of the two metrics is identical, and they can be regarded as providing effectively equivalent information on the second-order moment of the axis distribution. Full discussion of these results are again deferred to section 3.

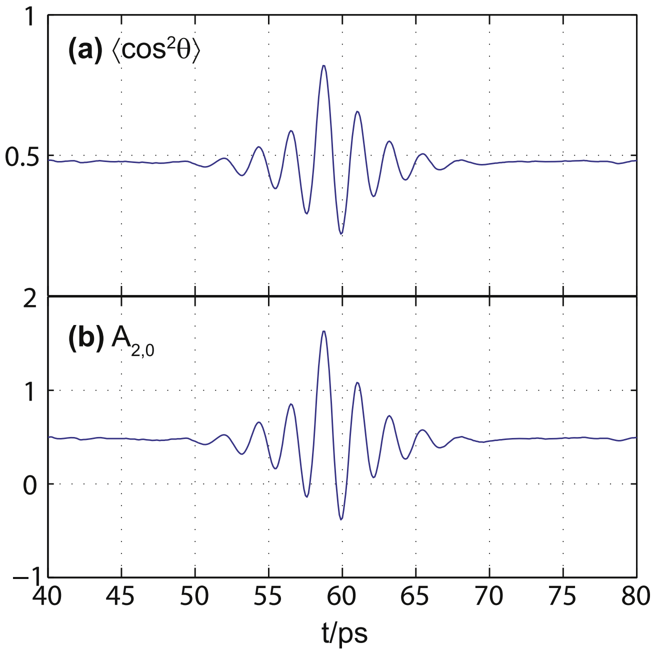

Figure 4. Alignment metrics (a) $\langle\cos^2(\theta,\ t)\rangle$ and (b) $A_{2,0}(t)$ corresponding to the $P(\theta, t)$ distribution shown in figure 3.

2.4. Ionization model

Here we consider the resulting photoelectron signal from ionization of an aligned distribution for a variety of cases. We begin with a full treatment of one-photon ionization, then generalize to the case of *N*-photon ionization, and finally discuss ionization via a resonant intermediate state. All these cases are typical of contemporary experiments on aligned systems although, to the best of our knowledge, only the former has been treated in detail in the literature with regard to ionization of aligned ensembles. The treatment presented here also includes frame rotations between the aligned frame and the probe frame, allowing for treatment of polarization-based methodologies such as angle-resolved ATI [21].

In all cases the aligned distribution is assumed to be created via an intense IR pulse which prepares a broad rotational wavepacket as described above. The resulting distribution $P(\theta, t)$ is described in terms of ADMs, i.e. as a geometric parameter, as detailed above. Ionization is treated within the dipole approximation, hence the ionization matrix elements have the general form $\langle\Psi^+;\ \Psi^e|\mu.\ \mathbf{r}|\Psi^i\rangle$, and describe the dipole coupling of the initial state Ψ^i to the final composite state, composed of ion and photoelectron. By expanding the ionization matrix elements in terms of angular and radial functions most of the geometric coupling of the ionization matrix elements can be described analytically, allowing for certain, molecule-independent, properties and phenomena to be determined [38].

Treating the distribution geometrically is valid for the ionization step providing that (a) rotations are separable from the vibronic wavefunction, hence there is no coupling between rotational dynamics and other molecular properties; (b) the energy-dependence of the ionization matrix elements is negligible over the span of rotational levels populated; (c) that the ionization laser pulse can be treated as constant over the energy span of the rotational wavepacket, allowing all initially populated rotational states to be coupled into the ionization. Under these approximations the angular momentum coupling can be solved analytically [39]. In the case of ionization schemes involving more than a single photon this stipulation should also hold provided there are no dynamics in the intermediate state(s) on the time-scale of rotational motion[5]. For direct *N*-photon ionization via virtual states on the time-scale of the laser pulse (typically < 100 fs), this is expected to be a valid approximation. For the case of ionization via a resonant intermediate—a typical scheme in pump–probe type experiments investigating excited state molecular dynamics—this condition may be broken depending on the time-scales involved. In such cases, an explicit treatment of the rotational wavepacket on the excited state would be required to fully account for the evolution of $P(\theta, t)$ on the time-scale of the experiment, but a sudden-type approximation without inclusion of these additional dynamics may still provide a reasonable starting point. Finally, we note that the treatment given here assumes that the light–matter interaction is perturbative, so does not allow for field intensity effects. As such, it is not generally valid for strong-field ionization but, geometrically, should still provide useful insight to angle-resolved measurements at low computational cost.

---

[5] This is essentially the sudden approximation as applied to rotational motions.

2.4.1. One-photon ionization

The one-photon case has been extensively treated in the literature [28, 30, 39, 41]. We recount here the salient details, with a specific focus on the coupling of the observable to the $A_{K,Q}$, then proceed to determine the properties of specific types of measurement and extend the formalism to the N-photon case.

The full photoelectron angular distribution can be most generally expressed as a multipole expansion (analogous to $P(\theta, \phi, t)$ discussed above, see equation (2)):

$$I(\theta, \phi, t) = \sum_{L,M} \beta_{L,M}(t) Y_{L,M}(\theta, \phi). \tag{12}$$

Here the polar coordinates reference the LF, as defined by the probe pulse (see figure 1(d)), in which the photoelectron flux as a function of angle and time is measured[6]. The LF $\beta_{L,M}(t)$ can be written in terms of the coherent square of the dipole matrix elements: for the ionization of an aligned ensemble, in the perturbative and dipole approximations, and assuming that all time-dependence is contained in the axis distribution, the $\beta_{L,M}(t)$ can be written as [28, 39]:

$$\begin{aligned}\beta_{L,M}(t) = {} & (2L+1)^{1/2} \sum_{P} (-1)^{P} \begin{pmatrix} 1 & 1 & P \\ p & -p & R \end{pmatrix} e_{-p} e^{*}_{-p} \\ & \times \sum_{K} \sum_{Q} (2K+1)^{1/2} \begin{pmatrix} P & K & L \\ Q-M & -Q & M \end{pmatrix} A_{K,-Q}(t) \\ & \times \sum_{q,q'} (-1)_{q'} \begin{pmatrix} 1 & 1 & P \\ q & -q' & q'-q \end{pmatrix} \begin{pmatrix} P & K & L \\ q-q' & q'-q & 0 \end{pmatrix} \\ & \times \sum_{l,l'} \sum_{\lambda,\lambda'} (-1)^{\lambda'} (2l+1)^{1/2} (2l'+1)^{1/2} \begin{pmatrix} l & l' & L \\ \lambda & -\lambda' & M \end{pmatrix} \begin{pmatrix} l & l' & L \\ 0 & 0 & 0 \end{pmatrix} \\ & \times (-i)^{l'-l} \sum_{\Gamma,\Gamma'} \sum_{\mu,\mu'} \sum_{h,h'} b^{\Gamma\mu*}_{hl\lambda} b^{\Gamma'\mu'}_{h'l'\lambda'} \boldsymbol{D}^{\Gamma\mu*}_{hl}(q) \boldsymbol{D}^{\Gamma'\mu'}_{h'l'}(q'). \end{aligned} \tag{13}$$

The first line of equation (13) describes the polarization state of the ionizing radiation; the photon carries 1 unit of angular momentum with projection p onto the lab frame z-axis. For linearly polarized light aligned with the LF z-axis $p = 0$, hence from the 3-j symbol $P = 0, 2$ and $R = 0$. The spherical tensor components e_{-p} describe the polarization and amplitude of the ionizing radiation, for the case of linearly polarized light along the z-axis $e_{-p} = e_0 = e_z$ and the term $e_z e_z^*$ can be set to equal unity.

The second and third lines of equation (13) describe the convolution of the MF with the aligned axis distribution, $P(\theta, t)$, expressed as ADMs. The light field has MF projection terms q. Terms in $q = 0$ thus represent ionizing light polarized along the MF axis, while $q = \pm 1$ terms represent light polarized perpendicular to the MF axis. If the LF and MF are coincident then a single value of $q = p$ is selected, while an arbitrary rotation serves to mix terms in q as the LF polarization axis is projected onto different MF axis. This mixing (and averaging), due to the ADMs, is described by the coupling of P and K into the final multipole moments L.

The remaining lines of equation (13) deal with the photoelectron and 'molecular' terms. Here (l, λ) represent the photoelectron partial wave components [38, 47], with (orbital) angular momentum l, and MF projection λ. The terms $\boldsymbol{D}^{\Gamma\mu}_{hl}(q)$ represent the symmetrized radial components, with symmetrization coefficients $b^{\Gamma\mu}_{hl\lambda}$ (see appendix B), of the (radial) dipole matrix elements for each symmetry-allowed continuum Γ [39, 48, 49],

$$\boldsymbol{D}^{\Gamma\mu}_{hl}(q) = \left\langle \Psi^{+}; \psi^{\Gamma\mu,e}_{hl} \middle| \sum_{s} r_s Y_{1,q}\left(\hat{\mathbf{r}}_s\right) \middle| \Psi^{i} \right\rangle, \tag{14}$$

where $\psi^{\Gamma\mu,e}_{hl}$ are the partial wave components of the photoelectron wavefunction Ψ^{e} and the summation is over all electrons s. These matrix elements are complex, and may also be written in the form $\boldsymbol{D}^{\Gamma\mu}_{hl} = |\boldsymbol{D}^{\Gamma\mu}_{hl}| \mathrm{e}^{-\mathrm{i}\eta^{\Gamma\mu}_{hl}}$, where η is the total phase of the matrix element, often called the scattering phase. The radial matrix elements and phases are the only part of equation (13) which are not analytic functions and, in general, must be determined numerically [50, 51] or from experiment [52–54] for quantitative understanding of a given system. Symmetry-based arguments can, however, provide a means of determining which integrals are non-zero, hence which (l, λ) can appear in Ψ^{e}. Such considerations therefore allow for phenomenological, qualitative, or possibly semi-quantitative, treatments of photoionization for a given molecule, and are discussed in appendix B.

---

[6] Although omitted here, there is also an energy dependence to the dipole matrix elements and, hence, to the observable $I(\theta, \phi, t)$.

The effect of the averaging over a distribution of molecular axis directions is to lose sensitivity in the PADs. In particular, the observed anisotropy in the LFPAD cannot be more than that arising from the coupling of the probe photon to the aligned distribution of molecules, as can be seen from the 3-j term linking terms P, K, L. This limits L to the range $|P-K|\ldots P+K$ in integer steps. For instance, if the alignment is prepared by a single pump photon then a $\cos^2\theta$ axis distribution is created, and the only non-zero alignment parameters are $A_{0,0}$ and $A_{2,0}$. Because $P=0, 2$ only, the alignment in this case would restrict $\beta_{L,M}(t)$ to terms with $L=0, 2, 4$ (additionally, for cylindrically symmetric cases, $M=-Q=0$). As the degree of alignment increases higher-order K terms are required to describe the axis distribution and the LF ensemble result approaches the true MF [28]. Higher order terms in equation (13) can be observed, hence more information is present in the LFPAD and a greater sensitivity to any property which affects the PADs, e.g. the evolution of the axis distribution itself, intermediate state dynamics in a pump–probe experiment, and so on, may be obtained.

For an angle-integrated measurement (photoelectron yield), integration over $\{\theta, \phi\}$ leaves only the leading term $\beta_{0,0}(t)$, and angular coherences between partial waves are integrated out of the measurement. In this case the terms remaining in (13) are significantly restricted by the 3-j terms. Allowed terms have $l=l'$ and $P=K$. For instance, for one-photon ionization of a distribution with $P=0, 2$, only $A_{K,Q}(t)$ with $K=0, 2$ will be coupled to the ionization yield. Depending on the magnitudes of the parallel and perpendicular ionization matrix elements, this can result in the one-photon yield mapping the $A_{2,0}(t)$ somewhat directly [31].

To make the geometric convolution of the axis distribution and MF photoionization more explicit, equation (13) can also be written in the form [28]:

$$\beta_{L,M}(t) = \sum_{K,Q} A_{K,-Q}(t)\, a_{KLM}, \tag{15}$$

where the a_{KLM} contain all the other terms of equation (13). As per equation (13), the allowed values of M and Q are coupled; for cylindrically symmetric geometries, i.e. probe polarization parallel to the pump polarization, $Q=M=0$. In this case the photoelectron yield is given by:

$$\beta_{0,0}(t) = \sum_{K=0,2} A_{K,0}(t)\, a_{K00}, \tag{16}$$

$$= A_{0,0}(t)\, a_{000} + A_{2,0}(t)\, a_{200}. \tag{17}$$

Since the zero-order term $A_{0,0}(t)$ is just the total population of the rotational states forming the wavepacket (often normalized to unity), it is a constant in the absence of any population dynamics, and any time-dependence observed in the ionization yield is due to the second-order term, as asserted above.

The effect of frame rotations on the $\beta_{L,M}(t)$ can also be simply expressed using this form, and employing the Wigner rotation matrix:

$$\beta'_{L,M'}(t;\Omega) = \sum_{K}\sum_{Q,Q'} D^{K}_{Q',Q}(\Omega)\, A_{K,-Q}(t)\, a_{KLM}, \tag{18}$$

$$= \sum_{K}\sum_{Q'} A'_{K,-Q'}(t)\, a_{KLM'}, \tag{19}$$

where the second form follows from the assumption that $Q=0$. Here $\Omega=\{\Phi, \Theta, \chi\}$ is the set of Euler angles describing the frame rotation between the alignment field and the probe field, and the properties in the rotated frame are denoted by primes. The rotation mixes multipole components Q within a given rank K. Because of the coupling between Q and M (the second 3-j term in equation (13)) different terms, M', are allowed in the rotated frame. As discussed above, and illustrated in figures 1 and 2, such a frame rotation can break the symmetry of an initially cylindrically symmetric distribution, hence M' may be non-zero even if $M=0$.

Applying again the stipulations above, the ionization yield for a cylindrically symmetric distribution ($Q=0$) under a rotation of Θ between the alignment and ionization fields, is then given by:

$$\beta'_{0,0}(t;\Theta) = \sum_{K=0,2}\sum_{Q'} D^{K}_{Q',0}(0, \Theta, 0)\, A_{K,0}(t)\, a_{K00}, \tag{20}$$

$$= \sum_{K=0,2}\sum_{Q'} d^{K}_{Q',0}(\Theta)\, A_{K,0}(t)\, a_{K00}, \tag{21}$$

$$= A_{0,0}(t)\, a_{000} + d^{2}_{0,0}(\Theta)\, A_{2,0}(t)\, a_{200} + 2d^{2}_{2,0}(\Theta)\, A_{2,0}(t)\, a_{200}, \tag{22}$$

$$= A_{0,0}(t)\, a_{000} + \left(A'_{2,0}(t) + 2A'_{2,2}(t)\right) a_{200}, \tag{23}$$

where $d^K_{Q',Q}(\Theta)$ is the reduced Wigner rotation matrix element, and we have used the identities $d^0_{0,0} = 1$, $d^2_{2,0} = d^2_{-2,0}$ [55]. This form makes explicit the fact that the frame rotation mixes additional Q terms into $\beta'_{0,0}(t;\ \Theta)$ as compared to $\beta_{0,0}(t;\ \Theta = 0)$ (equation (17), see also figure 2). Therefore, in general, a measurement of $\beta'_{0,0}(t;\ \Theta \neq 0)$ will not map $A_{2,0}(t)$ as directly as $\beta'_{0,0}(t;\ \Theta = 0)$.

A measurement of the photoelectron yield as a function of Θ will therefore have the general form (using equation (3.93) from Zare [55]):

$$I(\Theta;\ t) = \beta'_{0,0}(\Theta;\ t) = A_{0,0}(t)a_{000} + \left(\frac{4\pi}{5}\right)^{\frac{1}{2}} A_{2,0}(t)a_{200}Y^{*}_{2,0}(\Theta,\ 0) + 2\left(\frac{4\pi}{5}\right)^{\frac{1}{2}} A_{2,0}(t)a_{200}Y^{*}_{2,2}(\Theta,\ 0). \tag{24}$$

Experimentally, this corresponds to a measurement of the photoionization yield as a function of polarization geometry (defined by Θ, as illustrated in figure 1(d)). Measurements of this form may be made for all Θ, yielding the polarization-angle-resolved ionization yield as a quasi-continuous function, or compared at selected Θ to provide 'transient anisotropy' measurements, for example the standard formulation (which compares yields at $\Theta = 0$ and $\Theta = \pi/2$) has been explored with respect to ionization [56]. Clearly, a polarization-resolved measurement of this form may be expected to display relatively complex angular structure, with up to four lobes on the interval $0 \leqslant \Theta \leqslant 2\pi$ due to the summation of $Y_{2,0}$ and $Y_{2,2}$ terms, despite the fact that only the second-order moment of the axis distribution is invoked. This serves to illustrate how even an apparently simple experimental measurement may respond in a more complex fashion than anticipated to an aligned ensemble.

2.4.2. Multi-photon ionization

Formally, a direct multi-photon ionization process constitutes a ladder of transitions through virtual states. In terms of the decomposition of this ladder of transitions into dipole matrix elements for each successive photon absorption—a direct extension of the one-photon case discussed above—the complexity rapidly grows, and may be further complicated by near-resonances with real bound states. A full treatment of such cases for atomic ionization has been given by Bebb and Gold [57], including the derivation of an effective N-photon matrix element to reduce the complexity of the problem[7]. Here we take a similar approach and consider treating the ionization as an effective one-photon transition in which the photon angular momentum is large. The ionization would then have a form essentially as equation (13), but with the photon carrying N units of angular momentum. Such a treatment should allow for at least a qualitative picture of the directionality of the ionization, and in particular the polarization-angle-resolved ionization yields $I(\Theta,t)$, with a clear link to the multipoles involved in the molecular axis alignment and ionization process.

The immediate result is that P can take many more values than in the one-photon case. For a cylindrically symmetric distribution equation (20) becomes:

$$\beta'_{0,0}(t;\ \Theta) = \sum_{K=0\ldots 2N} \sum_{Q'} D^K_{Q',0}(0,\ \Theta,\ 0)A_{K,0}(t)a_{K00}. \tag{25}$$

Hence higher-order ADMs may be coupled to the observed signal, according to the value of N. In practice one would expect, therefore, to observe more structure in the alignment trace (temporal signal) $\beta'_{0,0}(t;\ \Theta)$ for a given Θ, due to the coupling of larger K into the signal. Similarly, more angular structure may be observed in the angle-resolved yield $I(\Theta,t)$ and the PADs, $I(\theta,\ t;\ \Theta)$, recorded for a given polarization geometry. Because $l_{\max}$, the maximum photoelectron angular momentum, will also grow with N, it is likely that high-order ADMs are always coupled to such high-order processes, regardless of the exact details of the photoionization matrix elements.

Physically, one can understand the higher-order angular momenta as signifying a more directional ionization event. For example, in the limit of tunnel ionization, the outgoing electron is confined to a narrow angular spread by the shape of the tunnel, and one can envisage a jet of electron flux centred on the laser polarization axis[8]. In the framework of angular momentum theory, this is exactly equivalent to a process with high angular momentum. This is the same concept as discussed in section 2.1, where it was seen that contributions from larger angular momenta K give rise to a sharper, or more directionally localized, axis distribution. Ultimately, the angular-dependence of any observable, expressed in terms of an expansion in angular functions, can contain very high-order terms for processes which are highly directional.

---

[7] For more details see also Lambropoulos *et al* [73], who discussed many of the general issues in multi-photon ionization, including details of a range of formal treatments. Examples of the treatment of N-photon absorption for small N, in which all matrix elements are treated explicitly using a similar formalism to that employed in this work, can be found in, for example, [74–76]. A more recent treatment, including discussion of perturbative versus non-perturbative regimes, can be found in [77].

[8] Although, to reiterate a point already noted above, since a perturbative geometric treatment of the type shown here will not take intensity effects into account, for processes involving laser fields beyond the perturbative limit ($\gtrsim 10^{11}$ W cm^{-2}) it is best considered as a phenomenological comparator for the angular dependence of different polarization geometries and/or photon orders at a fixed intensity. Furthermore, this picture is somewhat of a simplification for complex systems, see for instance [78, 79].

2.4.3. Ionization via resonant intermediate states

The N-photon case discussed above assumed that all intermediate states were virtual and, consequently, did not provide any restrictions on the ionization. A distinctly different case arises when there is a single, or multiple, resonant intermediate state(s), because bound–bound transitions carry strict selection rules. In the context of this discussion we are concerned with the directionality, or polarization, of the bound–bound transition, as determined by the electronic dipole selection rules. Here we discuss the simplest case of a single bound–bound transition at the one-photon level prior to ionization—a $1+N$ resonantly enhanced multiphoton ionization (REMPI) process. The geometric formalism presented could readily be extended to more complex processes.

In the case of a one-photon bound–bound transition the initially prepared $P(\theta, t)$ will be raised by an additional power of $\cos^2(\theta)$ for a parallel transition, or $\sin^2(\theta)$ for a perpendicular transition, where the transition direction is defined by the symmetry of the bound states involved and the dipole operator. This can be considered purely geometrically, and the transition amplitudes are not required to model this process assuming only a single transition is allowed (or multiple transitions are resolved and can be considered independently). Strictly, such a transition will change the composition of the rotational wavepacket; however, under the assumption that there are no dynamics on the excited state (ionization is effectively instantaneous/rapid following excitation as compared to rotations as discussed above)—hence no rotational wavepacket propagation need be taken into account—then a geometric treatment is valid. Furthermore, the one-photon absorption contains coupling terms which change J by $0, \pm 1$, so will only minimally affect the envelope of a broad wavepacket.

In a purely geometric treatment, the axis distribution following a parallel transition is given by:

$$P'_{\parallel}(\theta, t) = \cos^2(\theta) P(\theta, t) \tag{26}$$

and for the perpendicular case by:

$$P'_{\perp}(\theta, t) = \sin^2(\theta) P(\theta, t) \tag{27}$$

The equation above can be written more explicitly in terms of the initial ADMs; for the parallel case we have:

$$P'_{\parallel}(\theta, t) = \cos^2(\theta) \sum_{K,Q} A_{K,Q}(t) Y_{K,Q}(\theta, \phi) \tag{28}$$

$$\propto \frac{1}{3}\Big(Y_{2,0}(\theta, 0) + 1\Big) \sum_{K,Q} A_{K,Q}(t) Y_{K,Q}(\theta, \phi), \tag{29}$$

where the $\propto$ arises because some normalization factors have been neglected. Similarly, for the perpendicular case we have:

$$P'_{\perp}(\theta, t) = \sin^2(\theta) \sum_{K,Q} A_{K,Q}(t) Y_{K,Q}(\theta, \phi) \tag{30}$$

$$\propto Y_{2,2}(\theta, 0) \sum_{K,Q} A_{K,Q}(t) Y_{K,Q}(\theta, \phi). \tag{31}$$

For cylindrically symmetric cases ($Q = 0$) and single photon ionization ($K = 0{,}2$) these equations simplify further to:

$$P'_{\parallel}(\theta, t) \propto A_{0,0}(t)\Big(1 + Y_{2,0}(\theta, 0)\Big) + A_{2,0}(t)\Big(Y_{2,0}(\theta, 0) + Y_{2,0}(\theta, 0)^2\Big) \tag{32}$$

and

$$P'_{\perp}(\theta, t) \propto A_{0,0}(t) Y_{2,2}(\theta, 0) + A_{2,0}(t) Y_{2,0}(\theta, 0) Y_{2,2}(\theta, 0), \tag{33}$$

where $Y_{0,0}(\theta, 0)$ has been assumed to be normalized to unity.

Hence, equation (17) becomes:

$$\beta^{\parallel}_{0,0}(t) = A_{0,0}(t) a_{000}\Big(1 + Y_{2,0}(\theta, 0)\Big) + A_{2,0}(t) a_{200}\Big(Y_{2,0}(\theta, 0) + Y_{2,0}(\theta, 0)^2\Big) \tag{34}$$

for the parallel case and, for the perpendicular case:

$$\beta^{\perp}_{0,0}(t) = A_{0,0}(t) a_{000} Y_{2,2}(\theta, 0) + A_{2,0}(t) a_{200} Y_{2,0}(\theta, 0) Y_{2,2}(\theta, 0). \tag{35}$$

As expected, in both cases higher-order angular moments appear in the observable, although only the second-order moment of the originally prepared $P(\theta, t)$ appears in the final equations. These equations show explicitly how resonant multi-photon ionization processes may respond to aligned ensembles in relatively complex ways, due both to the additional photon angular momentum coupled into the ionization and the angle-dependence of the resonant step. As was the case for frame rotations, such measurements respond to the $P(\theta, t)$ but in a less-than-direct manner, and this response is highly dependent on the nature of the probe process.

3. Application

Following from the theory outlined above, we explore the response of single and multi-photon ionization to molecular alignment for angle-integrated and angle-resolved measurements. We first consider the ADMs in detail, and discuss general features which might be expected for any molecular ensemble. Time-resolved ionization for a typical aligned ensemble, for various angle-integrated and angle-resolved measurements, is then discussed. Specifically, we consider the limiting cases of a one-photon probe and 1 + 1' REMPI scheme, both of which are common experimental techniques, w.r.t. both the axis distribution and the ionization matrix elements. For the multi-photon case we investigate the effect of N on the observables, as a function of the axis distribution, for a specific ionization process. These results should provide a general guide to experimentalists working with aligned distributions, since the order of the terms coupled into a given observable can significantly affect the experimentally measured quantities.

3.1. Axis distribution moments

3.1.1. General features

Calculation results for $P(\theta, t)$, in the region of the half-revival of a rotational wavepacket calculated for butadiene under typical experimental conditions, have already been illustrated in figure 3. The axis distributions were mapped in both Cartesian and polar space, and also expressed in terms of the associated second-order alignment metrics, $\langle\cos^2(\theta,\ t)\rangle$ and $A_{2,0}(t)$, in figure 4. As discussed above, and clear from the complex angular structure visible in figure 3, a full description of $P(\theta, t)$ requires higher-order moments of the axis distribution to be taken into account. Figure 5 illustrates this point with the temporal evolution of all ADMs up to $K = 40$ for this axis distribution. As already noted w.r.t. the $P(\theta, t)$ distributions, in this case it is clear that the degree of alignment is high, and many terms in K are significant in the $A_{K,Q}(t)$ expansion around the half-revival. Away from the peaks of the revival the degree of alignment is still high, due to an effective DC contribution to $P(\theta, t)$, although there are also high-frequency temporal modulations, particularly visible at the poles of the $P(\theta, t)$ distribution.

The $A_{K,Q}(t)$ which parametrize the full $P(\theta, t)$ distribution also show complex behaviour, as expected from the form of $P(\theta, t)$. Since we are concerned with the coupling of the aligned distribution—parametrized as a set of $A_{K,Q}(t)$—into an observable, we discuss here the evolution of the axis distribution in terms of the $A_{K,Q}(t)$ rather than the underlying rotational wavepacket. We also focus on the comparison of the higher-order terms with $K = 2$, since this corresponds to the most often used metric of alignment.

At the main peak of the alignment, $t \sim 59$ ps, all of the terms up to $K \simeq 24$ peak, reflecting the maximal axis alignment obtained at the half-revival. The widths of the features reveal a more complex temporal dependence of different order terms, with a narrowing of the revival peak at higher K. Immediately before and after this feature, at around $t \sim 58$ and $t \sim 60$ ps respectively, the traces show additional satellite features appearing at higher K. The satellite features around the half-revival have the effect of blurring out the anti-alignment features, relative to $K = 2$, hence would potentially reduce the observable contrast of the revival for an observable sensitive to higher-order terms as compared to a low-order observable. In general, it is clear that one would expect observables which couple to different order terms to exhibit different revival contrast and markedly different temporal evolution. Finally, it is worth noting that the frequency content of the distribution also scales with K (this is a direct consequence of terms with high ΔJ preferentially coupling into higher-order moments of the distribution). A high-order measurement away from the revival peak may, therefore, be difficult to interpret in terms of the expected (typically low-order) response and the complex temporal response may even be dismissed as experimental noise[9].

As compared with $\langle\cos^2(\theta,\ t)\rangle$, there is significantly more temporal structure in the higher-order K terms which is not coupled into $\langle\cos^2(\theta,\ t)\rangle$. This is clear from comparison of figure 4, which shows the direct correspondence between $\langle\cos^2(\theta,\ t)\rangle$ and $A_{2,0}(t)$. This follows from the overlap integral of equation (11) which, for $n = 2$, will be most significant for $K = 2$. Furthermore, the first few terms in K have similar temporal response to $K = 2$, and smaller magnitudes. The net result is that any contributions to the $\langle\cos^2(\theta,\ t)\rangle$ line-shape from these ADMs will have only a minimal effect on the overall temporal profile, and the $\langle\cos^2(\theta,\ t)\rangle$ metric can be considered as essentially equivalent to $A_{2,0}(t)$ in this case, as stated earlier (section 2.3) without explanation.

---

[9] There may also be a slight increase in numerical noise in the calculations for higher-order terms, although the smooth and explicable behaviour of the $A_{K,Q}(t)$ as a function of K implies this does not have a significant effect.

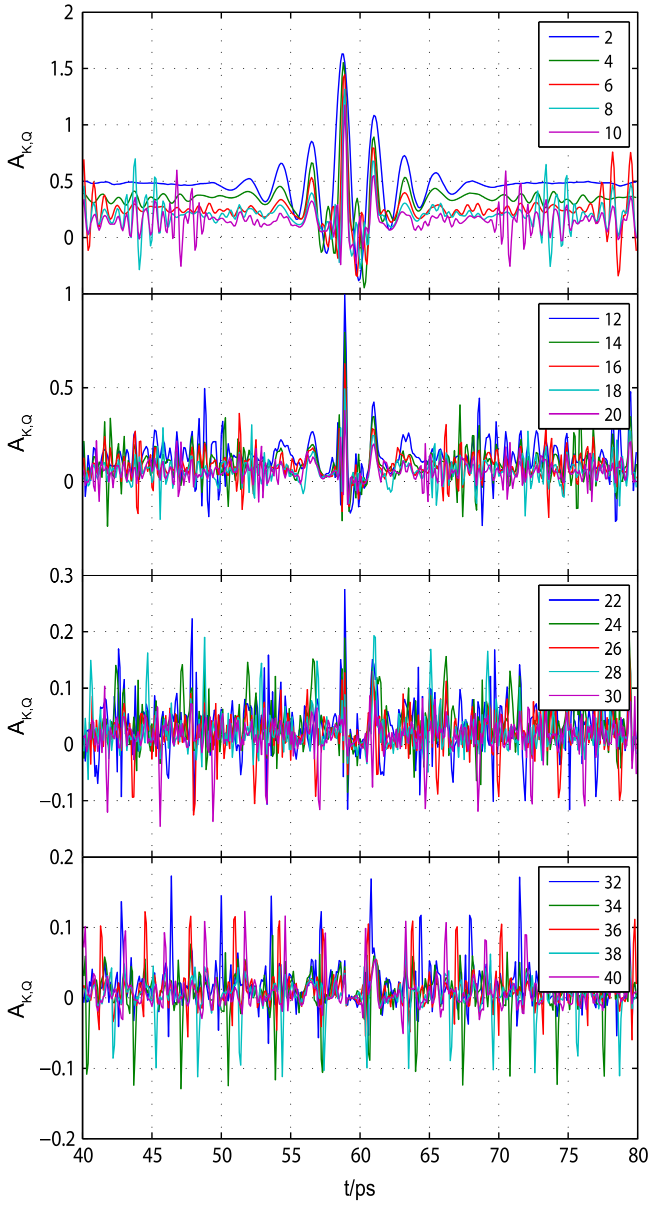

Figure 5. ADM expansion for calculated $P(\theta, t)$ as shown in figure 3. For clarity each plot shows only five $A_{K,0}(t)$ terms, and the expansion in K is only shown up to $K = 40$.

It may be concluded that, in general, a highly-aligned ensemble will contain high-order $A_{K,Q}(t)$ (effectively by definition), regardless of the precise details of the molecule under study. An appreciation for the coupling of this ensemble into the measurement is, therefore, essential for an understanding of experimental results. In particular, analysis of results based solely on $\langle\cos^2(\theta,\ t)\rangle$ will generally not be sufficient for interpretation of experimental data, even at a phenomenological level, beyond the simplest single-photon ionization yield probe scheme.

3.1.2. Resonant transitions

In order to treat the case of 1 + 1' REMPI, we consider distributions $P'_{\parallel}(\theta,\ t)$ and $P'_{\perp}(\theta,\ t)$ following parallel and perpendicular bound–bound transitions respectively, obtained via equations (26) and (27). These distributions are shown in figure 6. The parallel transition enhances the alignment, with a slight sharpening of the distribution at the poles (see figure 3), as might be intuitively expected from the form of equation (26). However, the perpendicular transition significantly changes the axis alignment. This is also an intuitive result: essentially the perpendicular transition couples preferentially to axes aligned in the $(x,\ y)$ plane, thus addressing only population away from the poles (z-axis) of the initial distribution. Consequently the peaks in the distribution are shifted both spatially (into the $(x,\ y)$ plane) and temporally, with the peak in the (x, y) plane of $P'_{\perp}(\theta,\ t)$

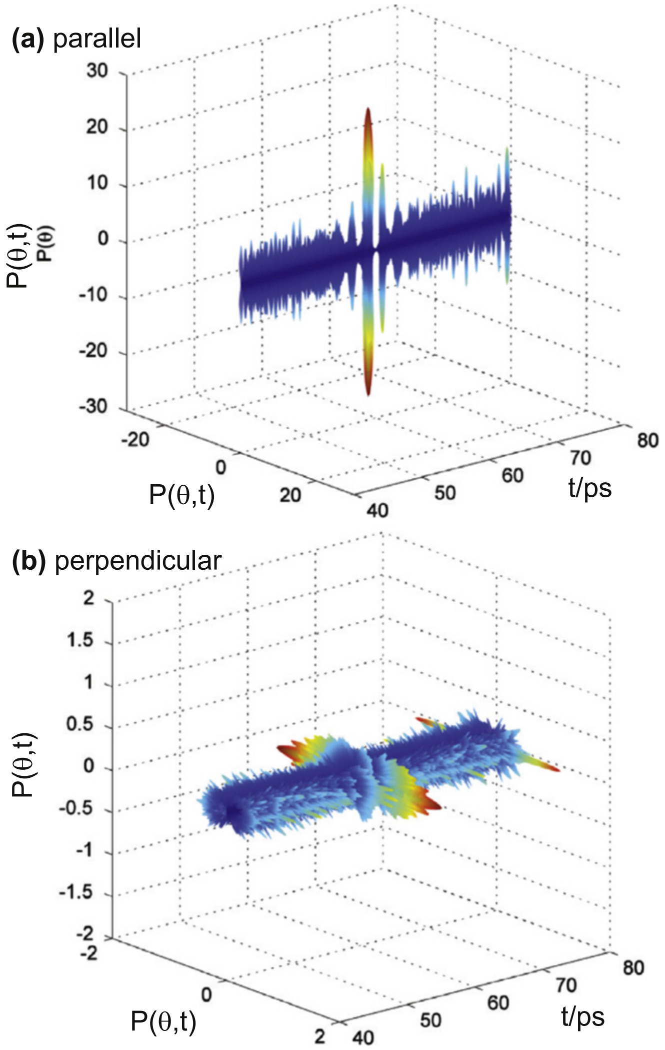

Figure 6. $P'(\theta,\ t)$ following (a) parallel and (b) perpendicular bound–bound transitions. These distributions are based on the initial distribution, $P(\theta, t)$, as shown in figure 3.

corresponding with the anti-alignment feature in the initial $P(\theta, t)$. As a consequence of the coupling, the high-order oscillations in the $(x,\ y)$ plane are, in effect, amplified.

Figure 7 illustrates these effects in terms of the ADMs and shows the $A_{K,Q}(t)$, up to $K = 10$, for both cases. In particular the effect of a parallel transition is to raise the second-order moment ($K = 2$) of the distribution, while a perpendicular transition will decrease the second-order moment. The temporal profiles are also affected, with the additional modulations appearing leading to significant temporal asymmetry in the $K = 2$ traces, particularly in the case of a perpendicular transition. Essentially the effect of the transition is to mix higher-order terms into a given K; for example the $A_{2,0}(t)$ trace for $P'_{\|}(\theta,\ t)$ has characteristics of both $A_{2,0}(t)$ and $A_{4,0}(t)$ of the initial $P(\theta, t)$—this can be seen by comparison of figures 5 and 7 (top panel). Because single photon ionization is only sensitive to $K = 0, 2$ terms of the aligned ensemble, as discussed above, the resonant excitation step has the effect of allowing $K = 4$ terms from the initial $P(\theta, t)$ to contribute to this observable since these are now mixed into the $A_{2,0}(t)$ ADMs for the excited state distribution $P'(\theta, t)$.

Again, in general one can conclude from this discussion that for more complex ionization processes higher-order terms become necessary to understand and interpret experimental results. In particular the perpendicular case illustrates how a process with strong selection rules (i.e. a highly directional response to the molecular axis alignment) acts as a strong filter on the initially prepared axis distribution. In the most general case of multiphoton ionization, where multiple resonances may be accessed sequentially or via different competing ionization pathways, it is clear that a very complex $P'(\theta, t)$ may be created which has little obvious correspondence to the initially prepared $P(\theta, t)$ and, without some appreciation of the underlying probe process, the temporal response of the observable may be inexplicable.

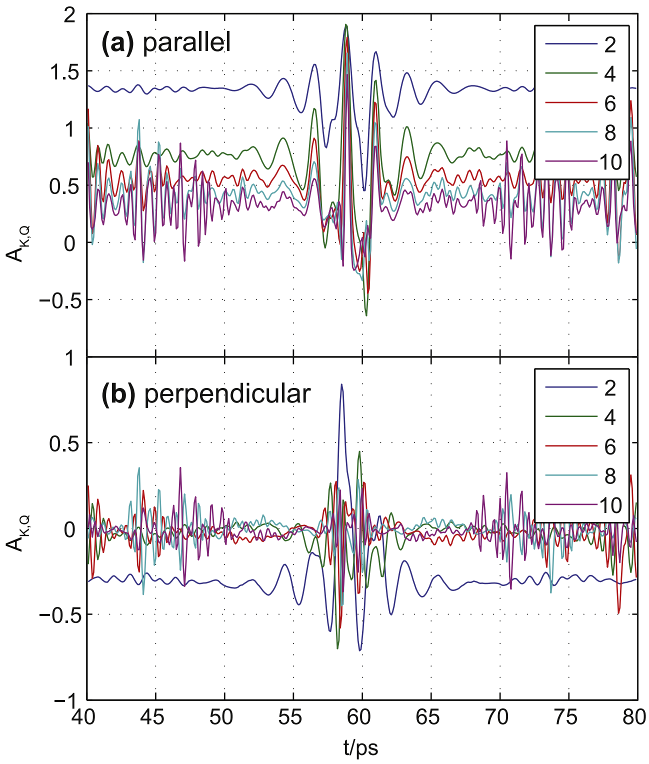

Figure 7. $A_{K,Q}(t)$ following one-photon excitation (shown for $K \leqslant 10$).

3.2. Angle-integrated observables

3.2.1. One-photon ionization yields

We first consider some limiting cases in order to investigate the response of the time-resolved photoelectron yield, $\beta_{0,0}(t)$, to $P(\theta, t)$. We consider the case of (a) one-photon ionization from the rotationally-excited ground state, (b) one-photon ionization following a parallel ($\cos^2(\theta)$) resonant excitation and (c) one-photon ionization following a perpendicular ($\sin^2(\theta)$) resonant excitation. The calculated $P(\theta, t)$ and the extracted $A_{K,Q}(t)$ for these cases have already been shown in figures 3, 5, 6 and 7, and discussed above. In all cases we assume that the probe (ionization) pulse polarization is parallel to the pump (alignment) pulse polarization, i.e. $\Theta = 0$. For the excitation step the laser pulse polarization is assumed to be either parallel or perpendicular to the alignment pulse polarization, as appropriate for the excitation, and its effect is treated geometrically (no temporal evolution of the wavepacket in the excited state) as discussed in section 2.4.3

The dipole matrix elements in equation (13) typically represent unknown quantities. In order to explore limitations on the ionization yield we consider the yield as a function of the parallel versus perpendicular ionization cross-sections ($\sigma_{\|}$ and $\sigma_{\perp}$). Specifically, in the case of butadiene—which is used here as an exemplar system—ionization of the S_2 excited state in C_{2h} symmetry leads to allowed continuum symmetries of A_g and B_g character for parallel and perpendicular ionization events respectively (see appendix B for details). The effect of varying the ratio of the ionization matrix elements is shown in figure 8. Here the matrix elements were set as

$$\boldsymbol{D}_{hl}^{\Gamma\mu} \equiv \sum_{q} \boldsymbol{D}_{|m|l}^{\Gamma}(q) = r\boldsymbol{D}_{|m|l}^{A_g}(0) + (1 - r)\boldsymbol{D}_{|m|l}^{B_g}(\pm 1)$$

and all symmetry-allowed terms, up to $l_{\max} = 4$, were included and set to unity. The matrix elements were further re-normalized such that $|\sum_{l,|m|} b_{|m|l|m|}^{A_g}\boldsymbol{D}_{|m|l}^{A_g}(0)|^2 = 1$ and $|\sum_{l,|m|} b_{|m|l|m|}^{B_g}\boldsymbol{D}_{|m|l}^{B_g}(\pm 1)|^2 = 1$. Hence $r = 1$ corresponds to the A_g continuum only, and a purely parallel ionization event in the MF, while $r = 0$ corresponds to the B_g continuum and a purely perpendicular ionization. Interestingly, the same type of calculation can also be used to extract the ratio of the matrix elements from experimental data by fitting of the matrix elements [30], although, due to the structure of equation (13), and as emphasized in equation (17), the $\beta_{0,0}(t)$ are sensitive only to the amplitudes of each l (although can contain cross-terms in λ), so phase information between different l is not defined, and cannot be obtained, from this observable alone.

These results—figure 8(a)—show quantitatively a number of features which might intuitively be expected. The ionization yield is sensitive only to $A_{2,0}(t)$, as shown in equation (17). For the purely parallel case ($r = 1$), the $A_{2,0}(t)$ is mapped faithfully (this is shown in detail in figure 9(a)), while the purely perpendicular case ($r = 0$)

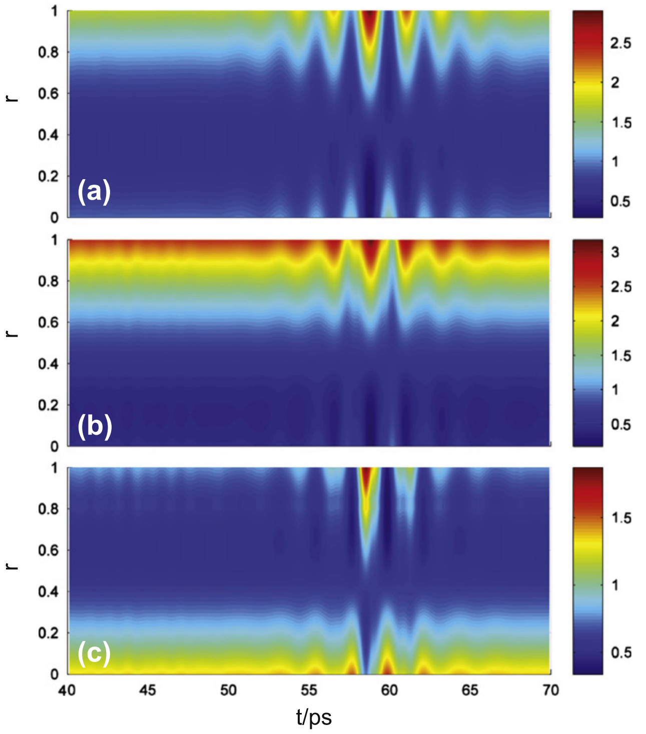

Figure 8. Limiting cases for one-photon ionization of an aligned distribution. Calculations are based on (a) calculated $P(\theta, t)$, (b) $P'_{\parallel}(\theta, t)$ for an excited state populated via a parallel one-photon transition and (c) $P'_{\perp}(\theta, t)$ for an excited state populated via a perpendicular one-photon transition. Ionization matrix elements are set such that $r = 0$ corresponds to a purely perpendicular ionization event, and $r = 1$ a purely parallel ionization.

shows an inverted trace, essentially mapping $\langle \sin^2(\theta, t) \rangle$. Additionally, the total yield is decreased in the perpendicular case due to the geometry—$P(\theta, t)$ is heavily peaked along the z-axis as shown in figure 3, so the axis distribution geometrically favours $q = 0$ transitions which are parallel to the molecular axis, hence aligned near to the LF z-axis. Between these limits, $0 < r < 1$, the ionization yield is less sensitive to the axis distribution, and even shows regions of no sensitivity where the balance of parallel and perpendicular components is such that there is no observable modulation in the yield. In other words, these are regions where there is no angular dependence for a second-order observable due to the equal magnitudes of parallel and perpendicular ionization cross-sections. The import of this is that, for a given molecule, it is possible that an observable sensitive to only the lowest order ADM shows no alignment dependence, despite the presence of an aligned distribution (see measuring at magic angle in order to cancel out $\cos^2(\theta)$ terms). Since this depends on a molecular property—the details of the ionization matrix elements—it is generally out of the control of the experimentalist, and may not be anticipated *a priori* unless the molecule under study is already well-characterized. Such a situation becomes less likely as higher-order moments are coupled to the observable.

Ionization yields following one-photon excitation, figures 8(b) and (c), show similar behaviour, with the main difference appearing due to changes in the temporal line-shapes of $P'(\theta, t)$ as discussed in section 3.1.2. The parallel yield following a parallel excitation, i.e. ionization of the distribution $P'_{\parallel}(\theta, t)$ with $r = 1$, is larger for all t (relative to case (a)), and is not modulated as strongly around the revival feature; conversely the perpendicular yield is reduced relative to case (a). The opposite is seen following a perpendicular excitation, i.e. ionization of the distribution $P'_{\perp}(\theta, t)$ (case (c)), which enhances the yield in the case of perpendicular ionization, and reduces it for parallel ionization. In both cases (b) and (c) this effect is due to the coupling of $K = 4$ terms from the initial axis distribution into the observable, as discussed above (section 2.4.3), and consequently also results in more complex temporal evolution of the signal, as would be expected from the form of the $A_{K,Q}(t)$ (figure 5). Despite this additional term, there are still values of r where the yield shows very little sensitivity to the ADMs, although the width of this region of r-space appears significantly reduced in the perpendicular case.

3.2.2. Multi-photon ionization yields

In the multiphoton case, as detailed in section 2.4.2, the expectation is for higher-order $A_{K,Q}(t)$ terms to become significant as the photon order of the process increases. This behaviour is illustrated in figure 9 for $N = 1 - 3$, and compared directly with the contributing $A_{K,Q}(t)$. In these calculations $r = 1$, hence the ionization is purely

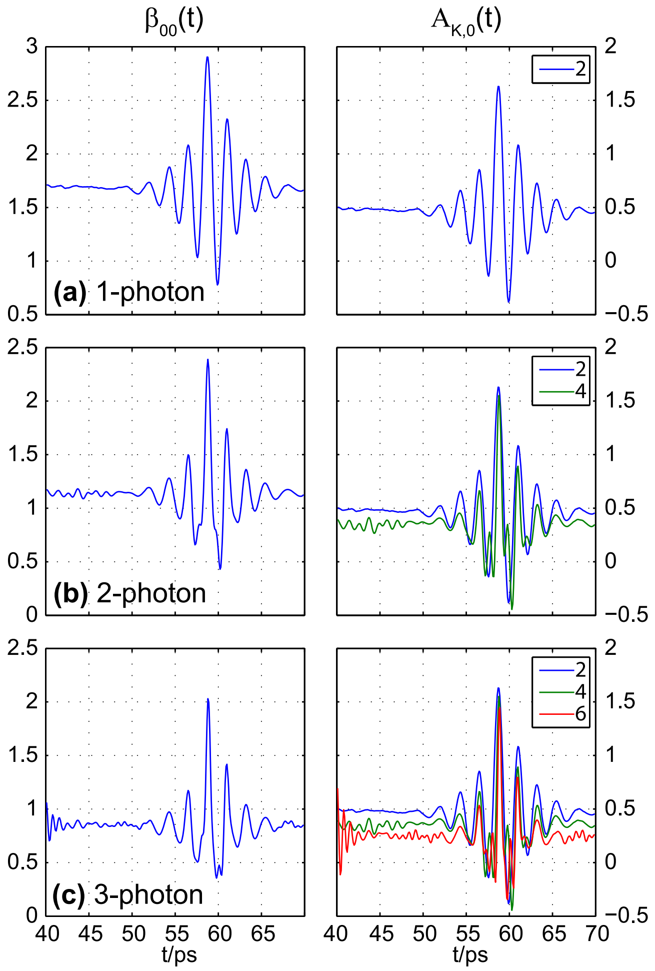

Figure 9. $\beta_{0,0}(t;\ \Theta)$ for N-order ionization processes. (Left column) $\beta_{0,0}(t;\ \Theta = 0)$ for $N = 1 - 3$ and (right column) $A_{K,0}(t)$ for $K_{\max} = 2N$.

parallel and, as for the one-photon case above, the probe and alignment pulse polarization are parallel ($\Theta = 0$). The line-outs show how the total ionization yield drops as a function of N, and also how the line-shapes change as couplings with larger K become allowed. Comparison of $\beta_{0,0}(t)$ with $A_{K,Q}(t)$ clearly shows that the line-shapes contain contributions from $A_{K,Q}(t)$ up to $K_{\max} = 2N$ (see also equation (25)): there is a narrowing of the features observed over the revival, and an increased complexity and temporal asymmetry to the line-shape as a function of N (equivalently as a function of $K_{\max}$), as already observed in the ADMs (section 3.1.1). The oscillations away from the revival also increase, again as expected from the $A_{K,Q}(t)$ traces. Naturally, the exact coupling will depend on both r (as illustrated for the one-photon case in the preceding section) and Θ (see below), but these general features will likely be apparent to some degree in an N-photon observable.

3.3. Angle-resolved observables

3.3.1. Angle-resolved ionization yields

Angle-resolved measurements, based on the response of the ionization yield to the probe polarization, are given by $\beta_{0,0}(\Theta,\ t)$ as defined in equation (25). This is essentially the same observable as discussed above—the total ionization yield, angle-integrated w.r.t. the photoelectron—except that measurements are made as a function of pump–probe polarization geometry, i.e. the angle Θ, as illustrated in figure 1(d).

Figure 10 shows surface plots for of $\beta_{0,0}(t;\ \Theta)$ for $N = 1 - 8$ and $\Theta = 0, 0.45, 0.95$ rad (0°, 26°, 54°) respectively (all other parameters were the same as those used in section 3.2.2); the data is re-normalized for each N to emphasize the changes in the line-shapes independently of the total yield. For ease of comparison, panel (a) shows the same results as figure 9 for $N = 1 - 3$, and the narrowing of the features with N, as discussed above, is again very clear. In cases (b) and (c) very different surfaces are observed, as expected from equation (25). The line-shapes are more complex, and this is particularly apparent in the splitting of the main feature observed for $N > 3$ in figure 10(b). As would also be expected, the 54° case shows reduced contrast as the aligned distribution is now rotated by close to $\pi/4$ from the probe pulse, hence the probe now maps a combination of $\langle \cos^K(\theta) \rangle$ and

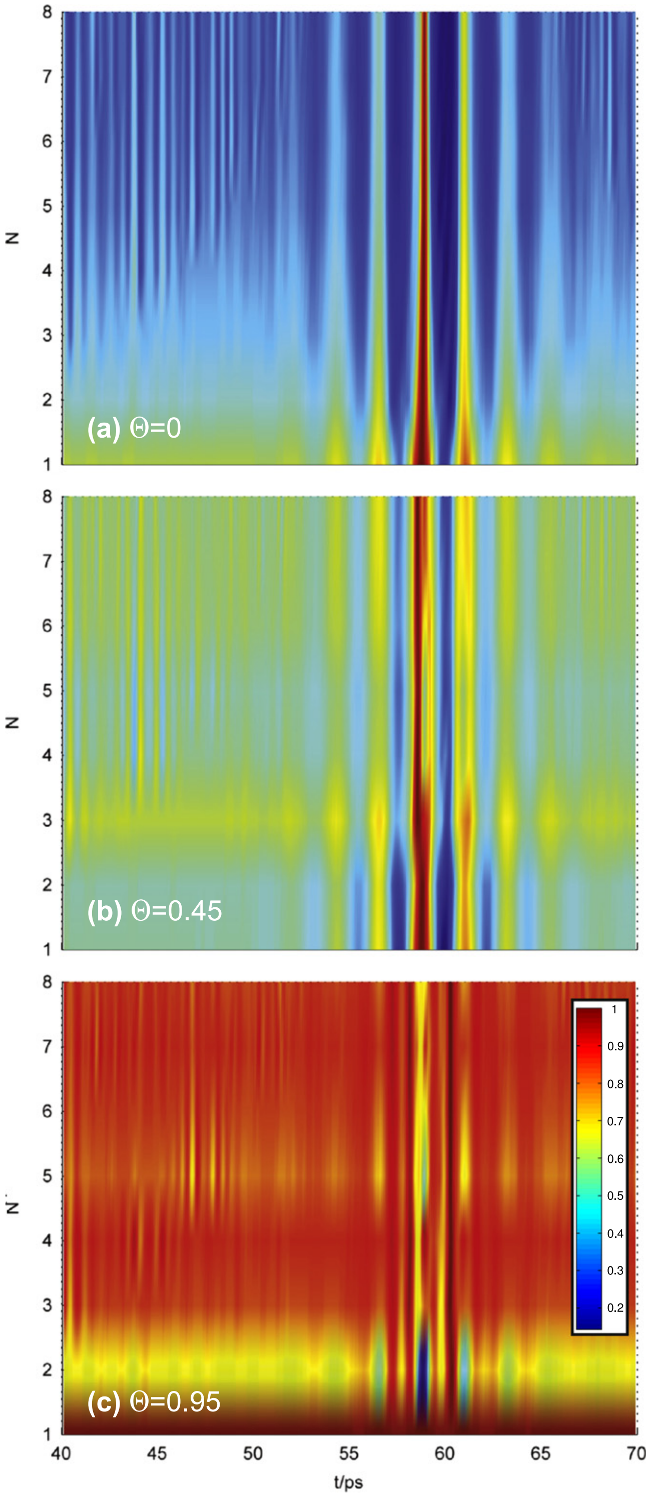

Figure 10. $\beta_{0,0}(t;\ \Theta)$ for N-order ionization processes. (a)$\beta_{0,0}(t;\ \Theta = 0)$ for $N = 1 - 8$, (b) as (a) but $\Theta = 0.45$ rad, (c) as (a) but $\Theta = 0.95$ rad. The surface plots are re-normalized to the peak of the signal for each N to emphasize the temporal behaviour.

$\langle \sin^K(\theta) \rangle$. For $N = 3$ in figure 9(b) and $N = 4$ in figure 9(c) a decreased sensitivity to alignment is observed. This is, presumably, due to the most geometrically significant $A_{K,Q}(t)$ term (most strongly coupled according to equation (25)) coming close to its magic angle, but may also be due to the distinct Θ-dependence of different order terms leading to regions where contrast is washed out. This is essentially the same effect discussed above, and shown in figure 9(c) for $\Theta = 0$ and $N = 3$, in which the t-dependence, rather than Θ-dependence, of different terms led to a decrease in revival contrast.

To further visualize this behaviour, figure 11 shows full surfaces of $I(\Theta,\ t)$ for $N = 1 - 3$ in polar form. These plots show more clearly the narrowing of the observed distributions at the poles as N increases. Comparison with

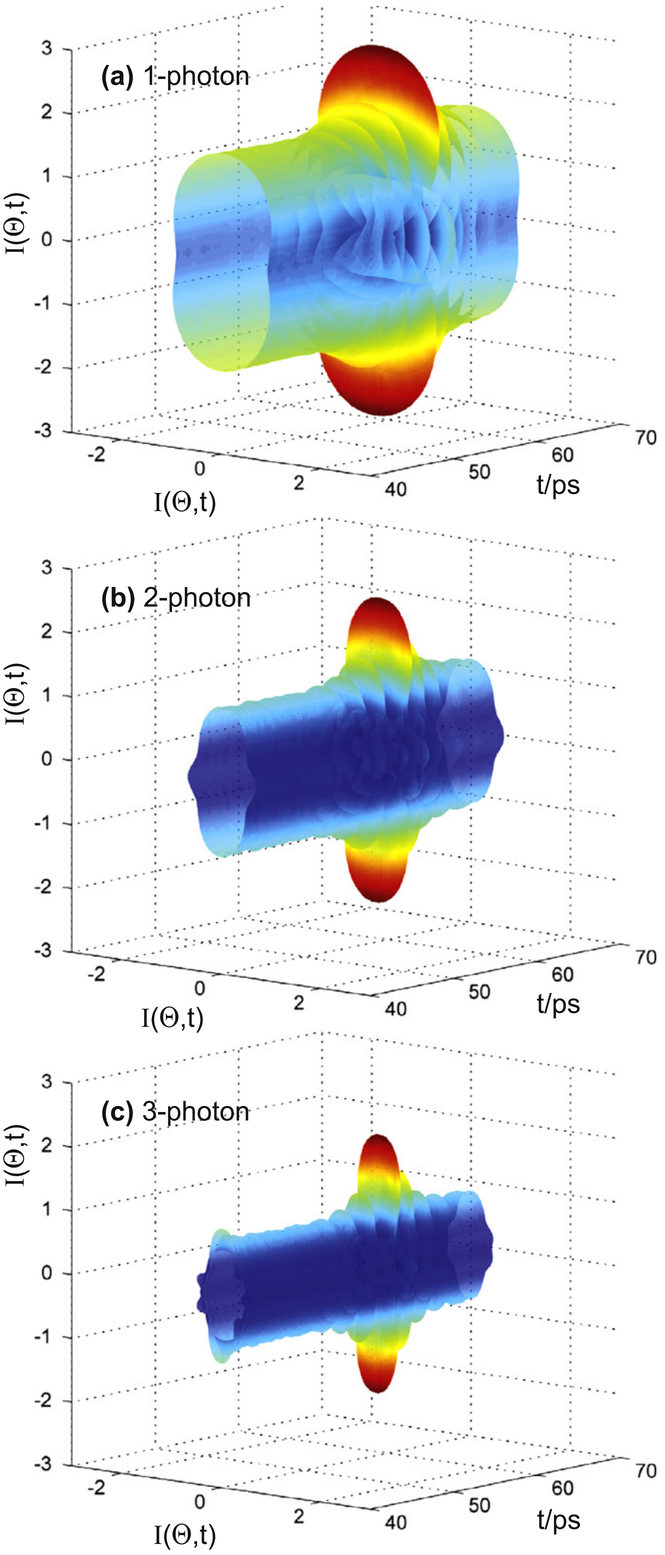

Figure 11. Polar plots of $I\ (\Theta,\ t)$ for $N = 1 - 3$.

figure 3(b) shows that the narrowing of the equator, as well as the increased spatial and temporal complexity, of higher N cases approach the full $P(\theta, t)$ surface—a direct result of higher $A_{K,Q}(t)$ terms becoming coupled into the observable, hence an increase in information content or fidelity w.r.t. the axis distribution. In this context, the most direct and detailed experimental measure for mapping an aligned distribution should be a multi-photon probe of high order, with terms up to $K_{\max} = 2N$ present in the observable in

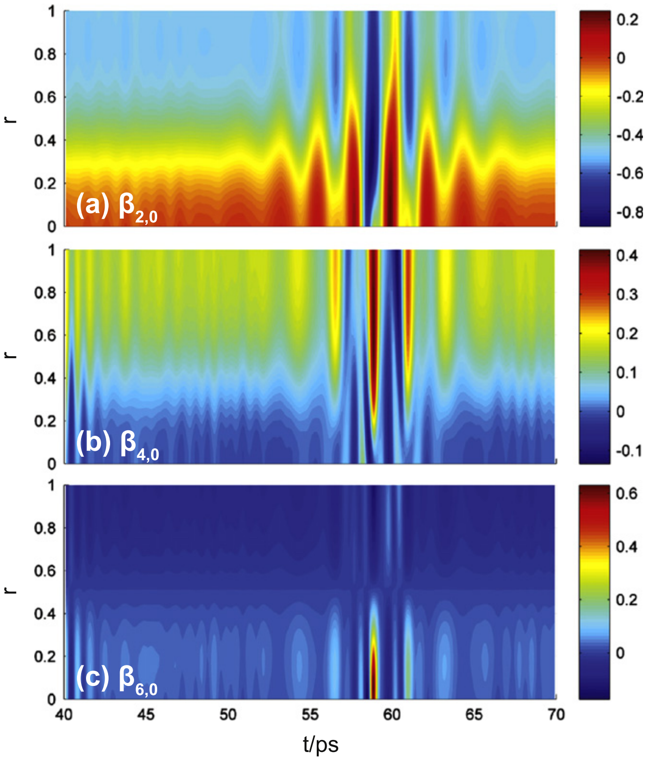

Figure 12. $\beta_{L,M}(t;\ \Theta = 0)$ for one-photon ionization, with (a) $L = 2$, (b) $L = 4$ and (c) $L = 6$; $M = 0$ in all cases. Ionization matrix elements are set such that $r = 0$ corresponds to a purely perpendicular ionization event, and $r = 1$ a purely parallel ionization, as per results already presented for $L = 0$ (ionization yield) in figure 8.

a—relatively—transparent manner, provided that the Θ-dependence of the probe process (i.e. the ionization matrix elements) is well-defined as in this illustration.

3.3.2. PADs

As was the case for the N-photon ionization yields discussed above, PADs can be considered as high-order observables with many $\beta_{L,M}(t)$ contributing to the observable. Hence, as indicated in equation (13), many $A_{K,Q}(t)$ may be mapped by the PAD. In terms of phenomenology, the extra sensitivity of the observed PAD to both the amplitudes and phases of the ionization matrix elements makes it difficult to choose realistic representative values for use in limiting case calculations. In this case we simply use the same limiting cases as above, i.e. $A_g + B_g$ continuum functions with amplitudes set to unity and phases set to zero, and explore the observables as a function of r. Generally, one could hope to obtain the matrix elements from experimental measurements of PADs if the alignment is known [8, 30, 31]; conversely, one could also use experimentally-measured PADs to map alignment in the case where the ionization matrix elements are known [27, 58].

Figure 12 shows examples of $\beta_{L,M}(t;\ \Theta = 0)$ calculated for these example cases, as a function of r as per the results discussed in section 3.2.1 and shown in figure 8. Similarly to the $I(\Theta,\ t)$ for N-photon ionization discussed above, higher-order L terms couple to higher-order K, resulting in more complex line-shapes which map primarily different $A_{K,Q}(t)$ as a function of L. One immediate result is that, with the exception of $r = 0.5$ and $L = 6$, there are no regions totally insensitive to the axis alignment in this case, in contrast to the $L = 0$ results shown in figure 8(a). Additionally, the higher-order terms are sensitive to the phases of the ionization matrix elements, so will display a much enhanced sensitivity to molecular properties (e.g. vibronic dynamics) as compared to the yields ($L = 0$) alone. Another interesting observation in this particular case is that the temporal peak in the $\beta_{2,0}(t)$ (at the half-revival) does not move significantly with r, although it does narrow and shift slightly. This is very different to the ionization yield, where the observable essentially mapped $A_{2,0}(t)$ for $r = 1$ (parallel ionization) but was inverted for $r = 0$ (perpendicular ionization), hence the half-revival feature appeared out of phase for $r = 0$ as compared to $r = 1$ (see figure 8(a)). However, for the $\beta_{4,0}(t)$ very different behaviour is observed, and there is a significant temporal shift in the main feature as a function of r, although the switch is not abrupt and does not occur at $r = 0.5$ as is the case for the yield (and as one might intuitively expect). Naturally, the specific details of these types of behaviour are highly dependent on the ionization matrix elements,

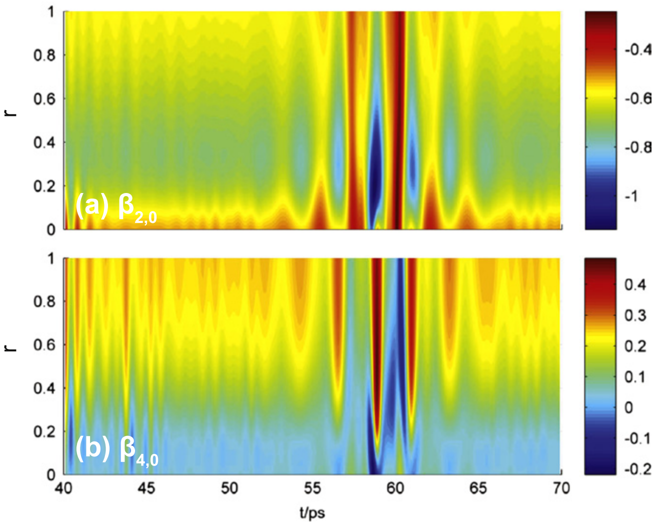

Figure 13. $\beta^{\parallel}_{L,M}(t;\ \Theta=0)$ for one-photon ionization, following parallel excitation, with (a) $L=2$, (b) $L=4$; $M=0$ in all cases. Ionization matrix elements are set such that $r=0$ corresponds to a purely perpendicular ionization event, and $r=1$ a purely parallel ionization, as per results already presented in figures 8 and 12.

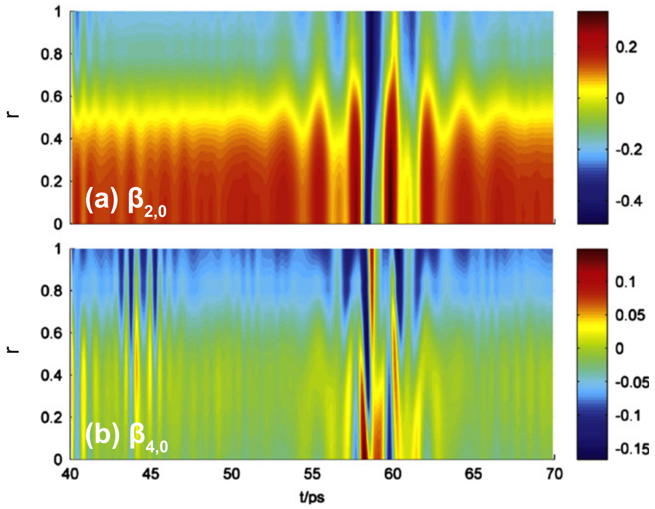

Figure 14. $\beta^{\perp}_{L,M}(t;\ \Theta=0)$ for one-photon ionization, following perpendicular excitation, with (a) $L=2$, (b) $L=4$; $M=0$ in all cases. Ionization matrix elements are set such that $r=0$ corresponds to a purely perpendicular ionization event, and $r=1$ a purely parallel ionization, as per results already presented in figures 8, 12 and 13.

but in general it is clear that a more complex temporal response is expected regardless of the exact details of the ionization matrix elements.

To further emphasize the sensitivity of the PADs to the ADMs, figures 13 and 14 show selected $\beta_{L,M}$ ($L=2$ and $L=4$) for ionization following one-photon absorption, for a parallel (i.e. axis distribution given by $P'_{\parallel}(\theta,\ t)$) and perpendicular (i.e. axis distribution given by $P'_{\perp}(\theta,\ t)$) absorption; in the following discussion we denote the $\beta_{L,M}(t)$ correlated to these cases as $\beta^{\parallel}_{L,M}(t)$ and $\beta^{\perp}_{L,M}(t)$ respectively. As expected, all of the $\beta_{L,M}$ respond to the change in the ADMs following absorption, and are much more sensitive to the details of the axis distribution than the yields alone (section 3.2.1). In particular:

- Higher-order terms become more strongly coupled. This is apparent from, for instance, the appearance of strong modulations in the $\beta_{2,0}(t)$ around 40–45 ps, far from the main half-revival feature, and the increase in contrast of such features in the $\beta_{4,0}$.

- The range and magnitudes of the $\beta_{L,M}$ change. Interestingly, for the set of matrix elements used here, $\beta_{2,0}^{\parallel}(t)$ has only negative values for all (t, r), while the sign of $\beta_{2,0}^{\perp}(t)$ changes at $r \sim 0.5$ (except at the half-revival feature). In both cases the average value of $\beta_{2,0}(t)$ for a given r is significantly different from ionization of the initial distribution $P(\theta, t)$; the range of $\beta_{L,M}$ values is similar for ionization of $P(\theta, t)$ and $P'_{\parallel}(\theta, t)$, although offset, but much reduced for $P'_{\perp}(\theta, t)$ (this is particularly evident for $\beta_{4,0}^{\perp}(t)$). Experimentally this would mean less significant changes in the time-resolved PADs would be observed in the latter case.
- The position of the temporal maxima, as noted above, move only slightly as a function of r for $\beta_{2,0}(t)$, but do move significantly for $\beta_{4,0}(t)$. Additionally, for $\beta_{2,0}^{\parallel}(t)$, the width and magnitude of the temporal maxima at the half-revival is almost constant for all r; this is quite distinct from the other cases.
- For $\beta_{4,0}^{\perp}(t)$ the line-shapes over the half-revival are more complex for all r, this is distinct from the behaviour observed for $\beta_{4,0}^{\parallel}(t)$ and all $L = 2$ cases, for which the half-revival features remain qualitatively similar in temporal complexity to the unexcited case. This change therefore reflects both the significant change in the ADMs for $P'_{\perp}(\theta, t)$ (see figure 7) and the enhanced coupling to higher-order ADMs for $L = 4$ as compared to $L = 2$.

These specific features indicate how complex the response of the $\beta_{L,M}(t)$ may be in any given case, with the temporal response reflecting both the ionization matrix elements and the ADMs. However, we again emphasize that one can begin to build some intuition on how these observables may respond phenomenologically to the ADMs and the experimental configuration in general terms, even if the precise details are molecule dependent. In this regard it is clear that one might expect a strong response to molecular alignment in all $\beta_{L,M}(t)$ as compared to the ionization yield (even in cases where the yield is insensitive to alignment), and that higher-order terms will contain higher-frequency components due to the coupling to higher-order ADMs.

This mapping has been discussed extensively by Seideman and co-workers (e.g. [30, 31]), including the possibility of extracting ionization matrix elements via fitting experimental data in this case. From an experimental perspective, measuring PADs may therefore be useful for characterizing alignment and ionization dynamics, but requires a rather involved analysis due to the high information content and complexity of the coupling [8]. However, the benefit of such measurements is precisely this high information content, so in some cases this effort is worthwhile. Similarly, in experiments where PADs are used as probes for other molecular properties (for a recent review of applications, see [59]), it is clear that the effect of rotational dynamics must be carefully considered precisely due to this complexity.

4. Discussion and conclusions

In general, from an experimental perspective, one can draw several qualitative conclusions from the results presented here, some obvious and some not so. Firstly, regardless of the degree of alignment achieved in a specific case, there is always the possibility that a given observable is insensitive to the alignment. In such cases one would often conclude that the experimental set-up is flawed in some way; however, as demonstrated in figure 8, at least in the one-photon case, there is a reasonable chance that the sensitivity of the photoelectron yield to alignment is small, or non-existent; for higher-order observables this is less probable, but contrast over the features of a revival may still be poor. Secondly, an observable sensitive to high-order terms may appear highly temporally structured, which could be inexplicable or even be attributed to experimental noise when considered in terms of expectations based on typical $\langle\cos^2(\theta, t)\rangle$ line-shapes but, if reproducible, is likely a valid result due to coupling of higher-order ADMs as illustrated in figure 5. Thirdly, high-order observables are required in order to map aligned distributions in detail, and multi-photon ionization is probably the cleanest probe to use to achieve the goal of mapping such distributions via ionization measurements.

Finally, following directly from these points, it is worth highlighting again that the low-order metrics in wide-spread use to describe aligned distributions (i.e. $\langle\cos^2(\theta, t)\rangle$) are of limited utility for a detailed description of the aligned distribution—and, consequently, the observable—in any case where higher-order terms are coupled to the observable under study. Experimentally, although one may not be interested in the details of the rotational wavepacket per-say, optimization of molecular axis alignment and appreciation of the effects it may have on an observable are certainly prerequisites to an optimal measurement, and for obtaining results which can be qualitatively, or even quantitatively, interpreted in terms of the molecular behaviour under study; clearly, even broad expectations about how a given signal may look are useful in this regard. These conclusions are also especially relevant to experiments aimed at measuring properties approaching the MF, since the coupling of the alignment moments of the distribution may be different from the true MF result even in the case of a high degree of alignment, and for time-resolved experiments where the time-scale of the evolution of the rotational distribution relevant to the experiment will depend on which alignment moments couple to the observable.

As a concrete example of this latter point, consider PADs obtained via a time-resolved pump–probe methodology, measured with the aim of studying the excited state molecular dynamics from a 'fixed-in-space' molecule [10, 60, 61]. In this case one must be careful to make pump–probe measurements on time-scales over which the alignment can be considered static, hence the temporal evolution of the rotational wavepacket will not play a role in the observable. However, what this time-scale is will depend on both the observable (i.e. whether higher-order terms play a role, see figure 5) and the details of the rotational wavepacket prepared, since a narrower rotational wavepacket will have broader temporal features (combined with a lower degree of alignment). This time-scale, in some cases, may be $\ll$ 1 ps, which is typical of the time-scales of (vibronic) molecular dynamics investigated in such pump–probe measurements, but is usually assumed to be 'safe' w.r.t. the time-scale of rotational wavepacket evolution. Without such considerations misleading conclusions are likely with, for example, alignment-mediated signal decays interpreted as state lifetimes, or changes in angle-resolved observables interpreted purely in terms of vibrational or electronic wavepacket evolution. Unfortunately such considerations do nothing to make alignment experiments easier, but do promise that more detailed and precise measurements can be made.

For completeness we reiterate that the treatment presented herein assumes a perturbative ionization regime (laser intensity $\lesssim 10^{11}$ W cm^{-2}), which in practice may be broken by the laser fields required to drive the high-order multi-photon processes of the kind suggested above for mapping aligned distributions. In such cases there may be modification of the rotational wavepacket during the ionization process, as well as the possibility of other strong-field effects; such considerations will naturally be very much molecule and laser wavelength dependent [62]. In general it should however be possible to drive few-photon processes, particularly in the UV, with perturbative fields, and some recent examples illustrating typical experimental conditions which drove various multi-photon processes in this regime can be found in [63–65]. Other recent work, [66], has demonstrated the possibility of combining perturbative and non-perturbative treatments at different photon-orders as one method of efficiently incorporating intra-pulse dynamics driven by an IR field in the moderate intensity regime 10^{12}–10^{13} W cm^{-2}) into photoionization calculations, hence presents a possible means to extend a geometric multi-photon treatment to the non-perturbative regime.

In this work various observables pertaining to single or few-photon ionization have been considered but, more generally, the same conclusions apply to other types of measurement, such as Coulomb explosion, high-harmonic generation [27] and x-ray diffraction [67], as well as more traditional measurements such as fluorescence. Of particular relevance in this regard is the recent article from Ramakrishna and Seideman [27], which explicitly considers rotational wavepacket imaging via different observables (Raman-induced polarization spectroscopy, one-photon ionization and high-harmonic generation) as a function of pump–probe geometry, so is highly complementary to the observables considered in this work. Simply put, without a detailed understanding of the couplings involved in a measurement one cannot hope to understand the details of either the prepared rotational wavepacket or the relation of the observable to the aligned distribution. This is an obvious conclusion, but is often ignored in experimental analysis—even at the phenomenological level—for reasons of simplicity. A recent illustration of the utility of a more complete experimental analysis is given in [15], where the observation of high-order rotational revivals in the high-harmonic signal from an aligned ensemble provided a way to determine the maximum continuum electron angular momentum, and further analysis also allowed the determination of the relevant matrix elements.

To summarize, in this work we have considered the coupling of highly-structured molecular axis distributions, typical of contemporary experiments utilizing strong IR pulses to prepare broad rotational wavepackets, into various types of photoionization measurement. The treatment highlighted the geometric complexity of the axis distributions created, and the role of the probe interaction in terms of the geometric coupling of the observable to the ADMs. Insight into the response of the observables was discussed in general terms, providing a phenomenology for a range of photoionization-based measurement schemes. Most generally, at a phenomenological level, this treatment indicates the types of complex behaviours which might be expected from *any* measurement technique which couples to high-order ADMs of an aligned molecular ensemble.

Acknowledgments

We are extremely grateful to Christer Z Bisgaard for providing mature code for the rotational wavepacket calculations used in this work. We thank Rune Lausten, Jochen Mikosch, Michael Spanner and Albert Stolow for helpful discussions on this topic and manuscript.

Table A1. Molecular parameters for butadiene. Literature values are taken from Craig *et al* [69] (experimental rotational constants) and Smith *et al* [70] (calculated static polarizabilities). Calculation column lists symmetrized values used in the rotational wavepacket calculations.

Property	Literature	Calculation (symmetrized)
A	1.3903772(6)cm^{-1}	1.3903772 cm^{-1}
	41.6831 GHz	41.6831 GHz
B	0.1478868(2)cm^{-1}	0.1408 cm^{-1}
	4.4335 GHz	4.2211 GHz
C	0.1336949(3)cm^{-1}	-
	4.0081 GHz	-
α_{zz}	12.82	12.82
α_{xx}	6.34	5.73
α_{yy}	5.12	-

Appendix A. Numerics

In the results detailed above, calculation of the axis alignment was made using code developed by C Z Bisgaard [43], as part of the work of H Staplefeldt's group. In these calculations the light–matter interaction is treated via a time-dependent Schrdinger equation (TDSE) formalism, in which the set of coupled differential equations are solved numerically by an adaptive-step Crank–Nicholson algorithm. This treatment requires knowledge of the (static) polarizabilities and the rotational constants of the molecule of interest, and the rotational temperature to determine the initial Boltzmann population of $|JKM\rangle$ states.

The Hamiltonian for the interaction with the laser pulse is given by [43]:

$$\hat{H}(t) = \hat{H}_{\text{rot}} + \hat{V}(t) = B\hat{J}^2 + (A - B)\hat{J}_z^2 - \frac{E(t)^2}{4}\left(\Delta\alpha\cos^2\theta + \alpha_\perp\right), \tag{A1}$$

where A and B are rotational constants, $E(t)$ is the (time-dependent) electric field, $\Delta\alpha$ is the difference between the parallel ($\alpha_\parallel$) and perpendicular ($\alpha_\perp$) polarizabilities, and $\hat{J}$ and $\hat{J}_z$ are the usual rotational operators for total rotational angular momentum and its projection onto the z-axis respectively.

After the laser pulse the c_J coefficients, that is the populations of the rotational states comprising the full rotational wavepacket, are fixed and field-free evolution of the wavepacket is determined analytically by equation (8). The axis distribution at time t is then calculated as per equation (6) which, making use of equation (7), can be written as [43]:

$$\begin{aligned} P(\Theta, t) = &\sum_J \left|c_J(t)\right|^2\left(J + \frac{1}{2}\right)\left(d^J_{-M,-K}(\Theta)\right)^2 \\ &+ \sum_{J<J'} 2\,\text{Re}\left(c_J(t)c^*_{J'}(t)\right)\left(J + \frac{1}{2}\right)^{\frac{1}{2}}\left(J' + \frac{1}{2}\right)^{\frac{1}{2}} d^J_{-M,-K}(\Theta)\, d^{J'}_{-M,-K}(\Theta), \end{aligned} \tag{A2}$$

where $d^{J'}_{-M,-K}(\Theta)$ are the (reduced) Wigner rotation matrix elements.

In the calculations the upper limit for J was set by the approximate scaling law determined empirically [43]:

$$J_{\max} = -0.35I^2 + 9.2I + 30, \tag{A3}$$

where I is the pulse (peak) intensity (in units of TW cm^{-2}).

Numerical results from a simplified version of this code, calculating only $\langle\cos^2(\theta, t)\rangle$ have previously been tested for a variety of cases [25, 43]. In this work the numerics of the calculation of the full $P(\theta, t)$ calculation were tested against the existing code by comparison of the $\langle\cos^2(\theta, t)\rangle$ parameters, i.e. by making use of equations (9) for 'direct' and (10) for 'indirect' or geometric calculations. This procedure was also tested for direct versus indirect calculation of $\langle\cos^4(\theta, t)\rangle$, providing confidence in the reliability of all other higher-order terms which were only extracted geometrically.

As noted above, in this work we considered butadiene as our exemplar system. The relevant molecular properties are given in table A1, which provides the literature values and the symmetrized values used in our calculations, which treat the molecule as a symmetric top. In this case, with the B and C rotational constants within 10%, this should be a reasonable approximation but, naturally, the numerical results illustrated here will not show any effects associated with asymmetric top rotational wavepacket dynamics [68]. Typical experimental conditions were used in our calculations, with $I = 5$ TW cm^{-2}, $\tau = 400$ fs, $T_r = 2$ K (rotational temperature).

Table B1. Butadiene symmetries and transitions. (a) State symmetries for the first three neutral states S_n, and first three ionic states D_n. (b) Multipole symmetries in C_{2h}. Characters correlate with different combinations of $(l,\ m)$, denoted by even (e) or odd (o). Dipole transition symmetries ($l = 1$) are also explicitly given in Cartesian form. (c) Allowed dipole transitions (one photon) and polarization, for bound–bound transitions $S_0 \rightarrow S_2$, and bound-free transitions to D_0 (ionic ground state). Bound-free transitions are labelled according to the continuum symmetry accessed for different dipole transition symmetries. As shown in (b), these symmetries correspond to different sets of partial waves.

State	Symmetry	Character	Dipole (Y_{1m})	Multipole (Y_{lm})		S_0	D_0
(a) State symmetries		(b) Multipole symmetries in C_{2h}			(c) Dipole transitions		
S_0	^1A_g	A_g		e, e	S_0	—	$B_u(z)$
S_1	^1A_g	B_g		e, o		—	$A_u(x,\ y)$
S_2	^1B_u	A_u	z	o, e	S_1	—	$B_u(z)$
D_0	^2B_g	B_u	$(x,\ y)$	o, o		—	$A_u(x,\ y)$
D_1	^2A_u				S_2	—	$A_g(z)$
D_2	^2A_g					(x, y)	$B_g(x,\ y)$

These conditions were chosen to correspond to recent experimental work on butadiene (which will be discussed in a later publication [42]). Extensive studies of rotational temperature effects and intensity averaging were not carried out in this case but, in general, it is expected that both effects will lead to a reduction in the maximum alignment, and a smoothing out of the temporal profile.

Appendix B. Symmetry

Symmetry plays a role in determining the allowed transition matrix elements and continuum wavefunctions. Here we treat the case of butadiene in its equilibrium planar geometry (C_{2h}), relevant to recent time-resolved experiments studying ultra-fast excited state dynamics from aligned butadiene, which utilized an IR alignment pulse followed by a 1 + 1' pump–probe measurement around the peak of the half-revival, to populate the S_2 state and probe the vibronic dynamics ([42]). These symmetries were used in the limiting case calculations presented in the main body of this manuscript.

Table B1 lists symmetries for (a) states of interest, (b) multipoles and (c) dipole transitions. The dipole-allowed $S_0 \rightarrow S_2$ transition accessed experimentally is (x, y) polarized, i.e. perpendicular to the molecular axis, so corresponds to a $\sin^2 \theta$ excitation as detailed in section 2.4.3. The excited state axis distribution $P'_{\perp}(\theta,\ t)$ is, therefore, distinctly different to the originally prepared $P(\theta, t)$. For one-photon ionization all dipole polarizations are symmetry allowed, but correspond to different continuum symmetries, hence different partial waves.

Ultra-fast population transfer from $S_2 \rightarrow S_1$ occurs in butadiene, and of particular note here is the switch from $g \rightarrow u$ continua for $S_2 \rightarrow D_0$ versus $S_1 \rightarrow D_0$, corresponding to a switch from even to odd l. In this case one would expect the PADs for these cases to be distinctly different.

As shown in table B1, the allowed continua correlate with different (l, m) even/odd combinations. To reduce the number of matrix elements, linear combinations of $\pm m$ can be used. In this case the $b_{hl\lambda}^{\Gamma\mu}$ symmetrization coefficients in equation (13) take values of 1 for $m = 0$, or $1/\sqrt{2}$ for $m \neq 0$. The indices are then reduced to the set $\Gamma = \{A_g,\ B_g\}, \mu = 1$ (no degenerate symmetries present), $h = |m|$ and $\lambda = |m|$.

Appendix C. Comparison with axis convolution methodology

Recent work has also considered a similar problem, where alignment was probed with a strong IR field [20, 25, 71] or via high-harmonic generation [17]. In these cases the ionization was treated purely geometrically as a (continuous) convolution of the form:

$$I\,(\Theta,\ t) = \iint P\,(\theta,\ t)\,S\,(\Theta)\,\sin\,(\theta)\,\mathrm{d}\theta\mathrm{d}\phi, \tag{C1}$$

where $S\,(\Theta)$ described the angular response of the signal to the angle between the aligning and probing laser fields, e.g. the angle-resolved ionization yield, and is given by an expansion in Legendre polynomials in the usual way:

$$S(\Theta) = \sum_L G_L P_L(\Theta). \tag{C2}$$

Conceptually this treatment is very similar to that given here, see equations (20) and (24), but treats the convolution numerically, and incoherently w.r.t. couplings between $P(\theta, t)$ and $S(\Theta)$, which are both here real valued functions by definition. For a cylindrically symmetric distribution, in which all terms in equation (24) are real, this simplification is valid. More generally (see equation (18)) this formalism will not correspond to the underlying (MF)properties of the signal, although it may be possible to find an angular response function $S(\Theta)$ which still models the observed signal $I(\Theta, t)$, as this has the form of a generic angular function. Therefore, an empirical convolution of this form, while mathematically valid in terms of the symmetry of the problem, should be treated with care if one is interested in determining physically meaningful properties.

Appendix D. Comparison with CS_2 formalism

In previous work on modelling the ionization of CS_2, specific equations were derived using a similar geometric treatment of the ionization yields arising from a 1 + 1' REMPI process, for both parallel and perpendicular excitation-probe geometries. The results were [10]:

$$I_{\parallel}(\theta, \phi) = I_0\Big[(r-1)\cos^4(\theta) + \cos^2(\theta)\Big], \tag{D1}$$

$$I_{\perp}(\theta, \phi) = I_0\Big[\cos^2(\theta) + (r-1)\cos^2(\theta)\cos^2(\phi) - (r-1)\cos^4(\theta)\cos^2(\phi)\Big], \tag{D2}$$

where $I_{\parallel}(\theta, \phi)$ and $I_{\perp}(\theta, \phi)$ are the angle-resolved ionization yields for a parallel and a perpendicular excitation-probe polarization geometry respectively, the angles (θ, ϕ) refer to the axis alignment relative to the ionization frame, I_0 is the total yield and r is the ratio of the parallel and perpendicular ionization dipole moments (similar to the definition used in section 3.2.1):

$$r = \left(\frac{\mu_{\parallel}}{\mu_{\perp}}\right)^2. \tag{D3}$$

These equations show explicitly that $\cos^4(\theta)$ terms contribute in this case. They also indicate the possibility of obtaining r if the alignment distribution is known, or the alignment distribution if r is known; or, possibly, fitting both in a self-consistent manner, as was demonstrated in that case based on the measured ratio of $\langle I_{\parallel}(\theta, \phi)\rangle$ to $\langle I_{\perp}(\theta, \phi)\rangle$ for an unaligned distribution, and the measured time-dependent yield for ionization from an aligned distribution using a parallel polarization geometry, $\beta^{\parallel}_{0,0}(t)$ in our notation (equation (34)). From the measurement the details of the prepared distribution were determined by the fitting procedure, where the free parameters were the peak intensity of the alignment pulse and the rotational temperature used in the rotational wavepacket calculations—hence the terms $\langle\cos^2(\theta, t)\rangle$ and $\langle\cos^4(\theta, t)\rangle$ were found by this fit. The full axis distribution $P(\theta, t)$ based on the best fit result was later used in modelling of the PADs [60]. Although we have not derived equivalent equations, we note that the angular terms are of the same order as those appearing in equations (34) and (35) when expressed in trigonometric form, so the formalisms may be assumed to be functionally identical.

References

[1] Seideman T 1995 *J. Chem. Phys.* **103** 7887
[2] Rosca-Pruna F and Vrakking M 2001 *Phys. Rev. Lett.* **87** 153902
[3] Renard V, Renard M, Guérin S, Pashayan Y, Lavorel B, Faucher O and Jauslin H 2003 *Phys. Rev. Lett.* **90** 153601
[4] Stapelfeldt H and Seideman T 2003 *Rev. Mod. Phys.* **75** 543
[5] Seideman T and Hamilton E 2006 *Adv. At. Mol. Opt. Phys.* **52** 289
[6] Reid K L, Field T A, Towrie M and Matousek P 1999 *J. Chem. Phys.* **111** 1438
[7] Tsubouchi M, Whitaker B J, Wang L, Kohguchi H and Suzuki T 2001 *Phys. Rev. Lett.* **86** 4500
[8] Suzuki T 2006 *Annu. Rev. Phys. Chem.* **7** 555
[9] Kumarappan V, Holmegaard L, Martiny C, Madsen C B, Kjeldsen T K, Viftrup S S, Madsen L B and Stapelfeldt H 2008 *Phys. Rev. Lett.* **100** 093006
[10] Bisgaard C Z, Clarkin O J, Wu G, Lee A M D, Gessner O, Hayden C C and Stolow A 2009 *Science* **323** 1464
[11] Holmegaard L *et al* 2010 *Nat. Phys.* **6** 428
[12] Maurer J, Dimitrovski D, Christensen L, Madsen L B and Stapelfeldt H 2012 *Phys. Rev. Lett.* **109** 123001
[13] Rouzée A, Kelkensberg F, Siu W K, Gademann G, Lucchese R R and Vrakking M J J 2012 *J. Phys. B: At. Mol. Opt. Phys.* **45** 074016
[14] Vozzi C, Negro M, Calegari F, Sansone G, Nisoli M, de Silvestri S and Stagira S 2011 *Nat. Phys.* **7** 822
[15] Lock R M, Ramakrishna S, Zhou X, Kapteyn H C, Murnane M M and Seideman T 2012 *Phys. Rev. Lett.* **108** 133901
[16] Lin C D, Jin C, Le A- T and Lucchese R R 2012 *J. Phys. B: At. Mol. Opt. Phys.* **45** 194010
[17] Bertrand J B, Wörner H J, Hockett P, Villeneuve D M and Corkum P B 2012 *Phys. Rev. Lett.* **109** 143001
[18] Frumker E *et al* 2012 *Phys. Rev. Lett.* **109** 233904

[19] Ren X, Makhija V, Le A-T, Troß J, Mondal S, Jin C, Kumarappan V and Trallero-Herrero C 2013 *Phys. Rev.* A **88** 043421

[20] Pavičić D, Lee K F, Rayner D M, Corkum P B and Villeneuve D M 2007 *Phys. Rev. Lett.* **98** 243001

[21] Mikosch J, Boguslavskiy A E, Wilkinson I, Spanner M, Patchkovskii S and Stolow A 2013 *Phys. Rev. Lett.* **110** 023004

[22] Dooley P W, Litvinyuk I V, Lee K F, Rayner D M, Spanner M, Villeneuve D M and Corkum P B 2003 *Phys. Rev.* A **68** 023406

[23] Lee K F, Villeneuve D M, Corkum P B, Stolow A and Underwood J G 2006 *Phys. Rev. Lett.* **97** 173001

[24] Küpper J *et al* 2014 *Phys. Rev. Lett.* **112** 083002

[25] Mikosch J, Bisgaard C Z, Boguslavskiy A E, Wilkinson I and Stolow A 2013 *J. Chem. Phys.* **139** 024304

[26] Hansen J L, Nielsen J H, Madsen C B, Lindhardt A T, Johansson M P, Skrydstrup T, Madsen L B and Stapelfeldt H 2012 *J. Chem. Phys.* **136** 204310

[27] Ramakrishna S and Seideman T 2013 *Phys. Rev.* A **87** 023411

[28] Underwood J G and Reid K L 2000 *J. Chem. Phys.* **113** 1067

[29] Suzuki Y-I, Tang Y and Suzuki T 2012 *Phys. Chem. Chem. Phys.* **14** 7309

[30] Ramakrishna S and Seideman T 2012 *J. Phys. B: At. Mol. Opt. Phys.* **45** 194012

[31] Suzuki Y-I and Seideman T 2005 *J. Chem. Phys.* **122** 234302

[32] Seideman T 1997 *J. Chem. Phys.* **107** 7859

[33] Seideman T and Althorpe S C 2000 *J. Electron Spectrosc. Relat. Phenom.* **108** 99

[34] Arasaki Y, Takatsuka K, Wang K and McKoy V 2001 *J. Chem. Phys.* **114** 7941

[35] Le A-T, Lucchese R R, Lee M T and Lin C D 2009 *Phys. Rev. Lett.* **102** 203001

[36] Abdurrouf A and Faisal F H M 2009 *Phys. Rev.* A **79** 023405

[37] Jin C, Le A-T, Zhao S-F, Lucchese R R and Lin C D 2010 *Phys. Rev.* A **81** 033421

[38] Dill D 1976 *J. Chem. Phys.* **65** 1130

[39] Stolow A and Underwood J G 2008 *Advances in Chemical Physics* ed S A Rice vol 139 (Hoboken, NJ, USA: Wiley) pp 497–584 ch 6

[40] Tang Y, Suzuki Y-I, Horio T and Suzuki T 2010 *Phys. Rev. Lett.* **104** 073002

[41] Seideman T 2002 *Annu. Rev. Phys. Chem.* **53** 41

[42] Hockett P and Stolow A 2015 in preparation

[43] Bisgaard C Z 2006 Laser-induced alignment *PhD Thesis* University of Aarhus (available at www.femtolab.au.dk/medias/media60.pdf)

[44] Artamonov M and Seideman T 2008 *J. Chem. Phys.* **128** 154313

[45] Underwood J G, Sussman B J and Stolow A 2005 *Phys. Rev. Lett.* **94** 143002

[46] Makhija V, Ren X and Kumarappan V 2012 *Phys. Rev.* A **85** 033425

[47] Messiah A 1970 *Quantum Mechanics* vol 1 (Amsterdam: North-Holland)

[48] Reid K L, Leahy D J and Zare R N 1991 *J. Chem. Phys.* **95** 1746

[49] Park H and Zare R N 1996 *J. Chem. Phys.* **104** 4554

[50] Lucchese R R, Raseev G and McKoy V 1982 *Phys. Rev.* A **25** 2572

[51] Arasaki Y, Takatsuka K, Wang K and McKoy V 1999 *Chem. Phys. Lett.* **302** 363

[52] Leahy D J, Reid K L and Zare R N 1991 *J. Chem. Phys.* **95** 1757

[53] Geßner O, Hikosaka Y, Zimmermann B, Hempelmann A, Lucchese R R, Eland J H D, Guyon P-M and Becker U 2002 *Phys. Rev. Lett.* **88** 193002

[54] Hockett P, Staniforth M, Reid K L and Townsend D 2009 *Phys. Rev. Lett.* **102** 253002

[55] Zare R N 1988 *Angular Momentum: Understanding Spatial Aspects in Chemistry and Physics* (New York: Wiley)

[56] Schalk O and Hockett P 2011 *Chem. Phys. Lett.* **517** 237

[57] Bebb H and Gold A 1966 *Phys. Rev.* **143** 1

[58] Reid K L and Underwood J G 2000 *J. Chem. Phys.* **112** 3643

[59] Reid K L 2012 *Mol. Phys.* **110** 131

[60] Hockett P, Bisgaard C Z, Clarkin O J and Stolow A 2011 *Nat. Phys.* **7** 612

[61] Wang K, McKoy V, Hockett P and Schuurman M S 2014 *Phys. Rev. Lett.* **112** 113007

[62] Lezius M, Blanchet V, Rayner D M, Villeneuve D M, Stolow A and Ivanov M Y 2001 *Phys. Rev. Lett.* **86** 51

[63] Vredenborg A, Roeterdink W G and Janssen M H M 2008 *J. Chem. Phys.* **128** 204311

[64] Hockett P, Ripani E, Rytwinski A and Stolow A 2013 *J. Mod. Opt.* **60** 1409–25

[65] Wilkinson I, Boguslavskiy A E, Mikosch J, Bertrand J B, Wörner H J, Villeneuve D M, Spanner M, Patchkovskii S and Stolow A 2014 *J. Chem. Phys.* **140** 204301

[66] Hockett P, Wollenhaupt M, Lux C and Baumert T 2014 *Phys. Rev. Lett.* **112** 223001

[67] Pabst S 2013 *Eur. Phys. J. Spec. Top.* **221** 1

[68] Holmegaard L, Viftrup S S, Kumarappan V, Bisgaard C Z and Stapelfeldt H 2007 *Phys. Rev.* A **75** 051403

[69] Craig N C, Davis J L, Hanson K A, Moore M C, Weidenbaum K J and Lock M 2004 *J. Mol. Struct.* **695-696** 59

[70] Smith S M, Markevitch A N, Romanov D A, Li X, Levis R J and Schlegel H B 2004 *J. Phys. Chem.* A **108** 11063

[71] Weber S J, Oppermann M and Marangos J P 2013 *Phys. Rev. Lett.* **111** 263601

[72] Felker P M and Zewail A H 1987 *J. Chem. Phys.* **86** 2460

[73] Lambropoulos P, Maragakis P and Zhang J 1998 *Phys. Rep.* **305** 203

[74] Bain A and McCaffery A 1984 *Chem. Phys. Lett.* **108** 275

[75] Dubs R L, McKoy V and Dixit S N 1988 *J. Chem. Phys.* **88** 968

[76] Docker M 1988 *Chem. Phys.* **125** 185

[77] Toffoli D and Decleva P 2012 *J. Chem. Phys.* **137** 134103

[78] Murray R, Spanner M, Patchkovskii S and Ivanov M Y 2011 *Phys. Rev. Lett.* **106** 173001

[79] Spanner M and Patchkovskii S 2013 *Chem. Phys.* **414** 10